Lai J, Chakraborty N, Lipatnikov AN.

Statistical behaviour of vorticity and enstrophy transport in head-on quenching of turbulent premixed flames.

European Journal of Mechanics - B/Fluids **2016**

DOI: http://dx.doi.org/10.1016/j.euromechflu.2016.10.013

Statistical behaviour of vorticity and enstrophy transport in head-on quenching of turbulent premixed flames

Jiawei Lai[1], Nilanjan Chakraborty[1*], Andrei Lipatnikov[2]

[1]School of Mechanical and Systems Engineering
Newcastle University
Newcastle-Upon-Tyne
NE1 7RU
United Kingdom
Email: j.lai@newcastle.ac.uk ; nilanjan.chakraborty@newcastle.ac.uk

[2]Department of Applied Mechanics
Chalmers University of Technology
Gothenburg, 412 96, Sweden
Email: andrei.lipatnikov@chalmers.se

[*] Corresponding author

ABSTRACT

The transport of vorticity and enstrophy in the near-wall region for head-on quenching of turbulent combustion by an isothermal inert wall has been analysed using three-dimensional Direct Numerical Simulation (DNS) data of statistically planar turbulent premixed flames characterized by various global Lewis numbers Le (ranging from 0.8 to 1.2) and turbulence intensities. In all cases the vorticity magnitude shows its maximum value at the wall and the vorticity magnitude drops significantly from the unburned to the burned gas side of the flame-brush. Moreover, the vorticity magnitude shows an increasing trend with decreasing Le, and increasing turbulence intensity. A significant amount of anisotropy has been observed between the vorticity components within the flame-brush and this anisotropy increases as the wall is approached. The baroclinic torque term has been found to be principally responsible for this anisotropic behaviour. The vortex-stretching and viscous dissipation terms remain the leading order contributors to the vorticity and enstrophy transport for all cases when the flame is away from the wall, but as flame approach the wall, the baroclinic torque begins to play an increasingly important role. The combined molecular diffusion and dissipation contribution to the enstrophy transport remains negative away from the wall but it changes its sign near the wall due to the torque arising from dilatation rate gradient. Detailed physical explanations have been provided for the observed influences of flame and wall on the statistical behaviours of vorticity and enstrophy and the various terms of their transport equations.

Keywords: Vorticity, Enstrophy, Head-on quenching, Lewis Number, Direct Numerical Simulation (DNS)

1. INTRODUCTION

Flame-wall interaction plays a pivotal role in determining the overall energy-efficiency, pollutant formation, as well as the durability and lifespan of combustors in industrial applications. Wall-bounded non-reacting flows have extensively been analysed using Direct Numerical Simulations (DNS) [1,2], but the analysis of flame-wall interaction [3-11] received relatively limited attention. The statistical behaviour of vorticity $\vec{\omega}$ and enstrophy $\Omega = \vec{\omega} \cdot \vec{\omega}/2$ plays an important role in the analysis of turbulent fluid motion [1,2], and these statistics are significantly affected by heat release, density variation and flame normal acceleration in turbulent premixed flames [12]. Several previous analyses focussed on the alignment of $\vec{\omega}$ with local principal strain rates in non-premixed [13-15] and premixed flames [16,17]. These analyses have demonstrated that $\vec{\omega}$ aligns predominantly with the intermediate principal strain rate similar to the non-reacting turbulent flows [18-28], but $\vec{\omega}$ also shows considerable alignment with the most extensive and compressive principal strain rates depending on the relative magnitudes of chemical and turbulent time scales. Chakraborty [17] has revealed that the global Lewis number Le (i.e. the ratio between thermal diffusivity α_T and mass diffusivity D) has significant influence on the alignment of $\vec{\omega}$ with local principal strain rates. The analysis by Chakraborty [17] revealed that $\vec{\omega}$ predominantly aligns with the intermediate and the most compressive principal strain rates for low Lewis number flames (e.g. $Le = 0.34$) where the dilatation rate remains almost equal to the most extensive principal strain rate.

The analysis by Hamlington *et al.* [16] has indicated that enstrophy $\Omega = \vec{\omega} \cdot \vec{\omega}/2$ drops from the unburned to burned gas side of flame-brush. On the contrary, Treurniet *et al.* [27] reported a localised increase of Ω within the flame-brush [29] for flames with high values of heat release parameter $\tau = (T_{ad} - T_0)/T_0$, where T_0 and T_{ad} are the unburned gas and the adiabatic flame temperatures respectively. Lipatnikov *et al.* [30] reported both generation and decay of

enstrophy across the flame brush in the cases of high (e.g. $\tau = 6.53$) and low (e.g. $\tau = 1.5$) values of heat release parameter, respectively. They also analysed the terms of the enstrophy and vorticity transport equation for weakly turbulent premixed flames in the corrugated transport flamelets regime. Recently, Chakraborty *et al.* [31] have demonstrated that Le significantly affects the baroclinic torque contribution to the enstrophy transport and this may lead to an augmentation of Ω within a flame for small values of Le under a turbulent flow condition in the unburned gas, contrary to a decay of Ω across the flame with $Le = 1.0$.

All the aforementioned analyses were conducted in configurations in the absence of walls. However, two-dimensional simulations by Poinsot *et al.* [3] of head-on quenching (HOQ) and three-dimensional incompressible channel flow DNS of side-wall quenching (SWQ) [4-7,9,10] of turbulent premixed flames revealed that the presence of wall significantly affects vorticity distribution near the wall. However, the statistical behaviours of vorticity $\vec{\omega}$ and enstrophy Ω transport in the presence of wall are yet to be analysed in detail. This paper addresses the aforementioned gap in existing literature by extracting the vorticity $\vec{\omega}$ and enstrophy Ω transport statistics from DNS data of HOQ of statistically planar turbulent premixed flames by an inert isothermal wall for different values of Lewis, Damköhler and Karlovitz numbers. The objectives of this analysis are:

(a) To demonstrate and explain the influences of wall on the statistics of $\vec{\omega}$ and Ω, and the terms of their transport equations,

(b) To identify the influences of Le on $\vec{\omega}$ and Ω statistics and their near-wall behaviour.

The rest of the paper will be organised as follows. The mathematical background and numerical implementation pertaining to this analysis are presented next. This will be followed by the presentation of the results and their subsequent discussion. The main findings will be summarised and conclusions will be drawn in the final section of this paper.

2. MATHEMATICAL BACKGROUND & NUMERICAL IMPLEMENTATION

The transport equation of the i^{th} component of vorticity $\omega_i = \varepsilon_{ijk}(\partial u_k/\partial x_j)$ is given by [29-31]:

$$\frac{\partial \omega_i}{\partial t} + u_k \frac{\partial \omega_i}{\partial x_k} = \underbrace{\omega_k \frac{\partial u_i}{\partial x_k}}_{t_{1i}} \underbrace{-\epsilon_{ijk} \frac{1}{\rho^2} \frac{\partial \rho}{\partial x_j} \frac{\partial \tau_{kl}}{\partial x_l}}_{t_{21i}} + \underbrace{\frac{\epsilon_{ijk}}{\rho} \frac{\partial^2 \tau_{kl}}{\partial x_j \partial x_l}}_{t_{22i}} \underbrace{-\omega_i \frac{\partial u_k}{\partial x_k}}_{t_{3i}} + \underbrace{\frac{\epsilon_{ijk}}{\rho^2} \frac{\partial \rho}{\partial x_j} \frac{\partial p}{\partial x_k}}_{t_{4i}} \quad (1)$$

where $\vec{u}$, ρ , p and $\tau_{kl} = \mu(\partial u_k/\partial x_l + \partial u_k/\partial x_l) - 2(\mu/3)\delta_{kl}(\partial u_m/\partial x_m)$ represent the velocity vector, gas density, pressure and stress tensor, respectively with μ being the dynamic viscosity. In Eq. 1, $\overrightarrow{t_1}$ is the vortex-stretching term, whereas $\overrightarrow{t_{21}}$ and $\overrightarrow{t_{22}}$ arise from the misalignment between the gradients of viscous stress and density and from the diffusion of vorticity, respectively. For constant dynamic viscosity (i.e. $\mu = \text{constant}$) incompressible flows, $\overrightarrow{t_{22}}$ becomes equal to $(\mu/\rho)\nabla^2\vec{\omega}$. However, for constant dynamic viscosity compressible flows, $\overrightarrow{t_{22}}$ takes the form $\overrightarrow{t_{22}} = (\mu/\rho)\nabla^2\vec{\omega} + (\mu/3\rho)\nabla \times \nabla(\nabla.\vec{u})$. The term $\overrightarrow{t_3}$ accounts for the dilatation contribution, and $\overrightarrow{t_4}$ is responsible for the baroclinic effects arising from the misalignment of the density and pressure gradients. Multiplying Eq. 1 by ω_i yields the transport equation for the enstrophy (i.e. $\Omega = \omega_i\omega_i/2$) [30,31]:

$$\frac{\partial \Omega}{\partial t} + u_k \frac{\partial \Omega}{\partial x_k} = \underbrace{\omega_i \omega_k \frac{\partial u_i}{\partial x_k}}_{T_1} \underbrace{-\epsilon_{ijk} \omega_i \frac{1}{\rho^2} \frac{\partial \rho}{\partial x_j} \frac{\partial \tau_{kl}}{\partial x_l}}_{T_2} + \underbrace{\frac{\epsilon_{ijk}\omega_i}{\rho} \frac{\partial^2 \tau_{kl}}{\partial x_j \partial x_l}}_{T_3} \underbrace{-2 \frac{\partial u_k}{\partial x_k} \Omega}_{T_4} + \underbrace{\epsilon_{ijk} \frac{\omega_i}{\rho^2} \frac{\partial \rho}{\partial x_j} \frac{\partial p}{\partial x_k}}_{T_5} \quad (2i)$$

The Reynolds-averaged enstrophy (i.e. $\bar{\Omega} = \overline{\omega_\iota \omega_\iota}/2$) transport equation can be obtained using Eq. 2i as [30,31]:

$$\frac{\partial \bar{\Omega}}{\partial t} + \overline{u_k \frac{\partial \Omega}{\partial x_k}} = \underbrace{\overline{\omega_i \omega_k \frac{\partial u_i}{\partial x_k}}}_{T_I} \underbrace{-\overline{\epsilon_{ijk} \omega_i \frac{1}{\rho^2} \frac{\partial \rho}{\partial x_j} \frac{\partial \tau_{kl}}{\partial x_l}}}_{T_{II}} + \underbrace{\overline{\frac{\epsilon_{ijk}\omega_i}{\rho} \frac{\partial^2 \tau_{kl}}{\partial x_j \partial x_l}}}_{T_{III}} \underbrace{-\overline{2 \frac{\partial u_k}{\partial x_k} \Omega}}_{T_{IV}} + \underbrace{\overline{\epsilon_{ijk} \frac{\omega_i}{\rho^2} \frac{\partial \rho}{\partial x_j} \frac{\partial p}{\partial x_k}}}_{T_V} \quad (2ii)$$

where $\bar{Q}$, $\tilde{Q} = \overline{\rho Q}/\bar{\rho}$ and $Q'' = Q - \tilde{Q}$ are the Reynolds-averaged, Favre-averaged and Favre fluctuation of a general quantity Q respectively. The term T_I indicates the vortex-stretching contribution, whereas T_{II} arises due to misalignment between gradients of density and viscous

stresses. The term T_{III} is responsible for molecular diffusion and dissipation of $\overline{\Omega}$, whereas T_{IV} and T_V represent the dilatation and baroclinic torque contributions respectively.

Under the assumption of constant dynamic viscosity, the dissipation rate $\tilde{\epsilon}$ of turbulent kinetic energy $\tilde{k} = \overline{\rho u_i'' u_i''}/2\overline{\rho}$ is closely related to enstrophy as: $\overline{\rho}\tilde{\epsilon} \approx 2\overline{\mu\Omega}$ in the isotropic Kolmogorov turbulence [32]. It has been demonstrated earlier [29,33,34] that the influences of a flame on the major statistical characteristics of a turbulent flow (such as $\tilde{k}$, $\tilde{\epsilon}$ and $\overline{\Omega}$) remain qualitatively similar in the cases of temperature-dependent and constant dynamic viscosity. This similarity stems from the fact that, due to a decrease in the density ρ with increasing temperature, the kinematic viscosity $\nu = \mu/\rho$ increases in flames under both conditions. Here the constant viscosity assumption is adopted for the purpose of simplicity. Under such conditions, the mean dissipation rate $\tilde{\epsilon}$ is directly proportional to the mean enstrophy $\overline{\Omega}$. Therefore, the understanding of $\overline{\Omega}$ transport is crucial for addressing the modelling of the dissipation rate of turbulent kinetic energy.

The chemical mechanism is simplified here by a single-step Arrhenius-type mechanism in order to analyse the effects of global Lewis number Le in isolation, following several previous analyses [17,38-52]. A single-step Arrhenius-type irreversible chemical reaction is chosen for the current analysis, because three-dimensional DNS simulations with detailed chemistry are extremely expensive for a detailed parametric analysis as carried out in this paper [53]. It is worth indicating that the head-on quenching of premixed flames by isothermal wall is principally driven by heat transfer and not by chemical mechanism [3-7]. Several previous DNS analyses on flame-wall interaction used a single step simplified chemical mechanism [3-7], and the same approach has been adopted here. Moreover, the statistical behaviours of vorticity and enstrophy transport in premixed turbulent flames are principally driven by fluid-

dynamics, and the pressure and density gradients induced by thermal field. These aspects are dependent on global dependences of chemical reaction rate on reaction progress variable and temperature fields, which are satisfactorily captured by single step simple chemistry (e.g. compare the reaction progress variable dependence of chemical reaction rate in Refs. [54] and [55]). Furthermore, the normalised values of wall heat flux and quenching distance obtained from single-step chemistry calculations [3,11] for head-on quenching of turbulent premixed flames based are found to be in good agreement with experimental findings [56-58].Thus, it can be expected that the present findings will at least be qualitatively valid.

The species field is represented by a reaction progress variable c, which is defined in terms of a suitable reactant mass fraction Y_R (e.g. $c = (Y_{R0} - Y_R)/(Y_{R0} - Y_{R\infty})$) so that c increases monotonically from 0 in the unburned gas to 1.0 in fully burned products. Here the computational domain of size $70.6\delta_Z \times 35.2\delta_Z \times 35.2\delta_Z$ is discretised using a uniform Cartesian grid of $512 \times 256 \times 256$ ensuring at least 10 grid points across the thermal flame thickness $\delta_{th} = (T_{ad} - T_0)/Max|\nabla\hat{T}|_L$. Here, $\delta_Z = \alpha_{T0}/S_L$, α_{T0}, S_L and $\hat{T}$ are the Zel'dovich flame thickness, thermal diffusivity in the unburned gas, unstrained laminar burning velocity and instantaneous temperature respectively. The mean direction of flame propagation is the negative x_1 −direction for this HOQ configuration. The boundary at $x_1 = 0$ is taken to be the no-slip isothermal wall with temperature $T_w = T_0$. The mass flux in the wall-normal direction is specified to be zero, and a partially non-reflecting boundary is considered for the face opposite to the wall. The boundary conditions are specified using the Navier Stokes Characteristic Boundary Condition (NSCBC) technique [59]. The transverse directions (i. e. x_2 and x_3) are considered to be periodic. High order finite-difference (10^{th} order central difference for the internal grid points and the order of accuracy gradually reducing to a one-sided 2^{nd} order scheme at the non-periodic boundaries) and Runge-Kutta (3^{rd} order low storage)

schemes have been used for spatial differentiation and explicit time advancement respectively. The strength of turbulent staining increases with decreasing length scale of turbulent eddies (i.e. increasing wave number), and thus it is important to have highly accurate spatial discretisation scheme to represent small-scale turbulent straining without any loss of accuracy (which happens for large wavenumbers for finite-difference schemes with smaller degree of accuracy). This requirement does not apply for temporal integration. The time step size is taken to be smaller than the Kolmogorov timescale and chemical timescale (i.e. δ_z/S_L) so all the significant time scales are resolved for these simulations. Thus, one does not need a very high order scheme for an accurate time integration. The same approach has been adopted in several previous analyses [30, 31, 38-52].

Three different global Lewis numbers (i.e. $Le = 0.8, 1.0, 1.2$) were considered for the current analysis. The Zel'dovich number $\beta = T_{ac}(T_{ad} - T_0)/T_{ad}^2$ (where T_{ac} is the activation temperature), Prandtl number Pr and the ratio of specific heats are taken to be 6.0, 0.7 and 1.4 respectively. The heat release parameter $\tau = (T_{ad} - T_0)/T_0$ is taken to be 6.0. The laminar flame used for initialising the combustion process is placed at a location where the influence of the wall is negligible (i.e. in these cases $(\hat{T} - T_0)/(T_{ad} - T_0) = 0.9$ isosurface for the unstrained planar laminar flame solution is kept a distance $20\delta_Z$ away from the wall) so that the flame gets enough time to evolve in the presence of turbulence before interacting with the wall. For the purpose of initialising the velocity field, an initially homogeneous isotropic field of the turbulent velocity fluctuations is generated using a pseudo-spectral method [60] following the Batchelor-Townsend Spectrum [61] but the velocity components u_1, u_2 and u_3 are specified to be zero at the wall to ensure no-slip condition. The velocity field is allowed to evolve for an initial eddy turn-over time (i.e. $t_e = l/u'$) before it interacts with the flame. For each Le, the simulations were conducted for the turbulence parameters shown in Table 1, which

presents the initial values of u'/S_L, ratio of integral length scale to flame thickness l/δ_{th}, Damköhler $Da = lS_L/\delta_{th}u'$ and Karlovitz $Ka = (u'/S_L)^{3/2}\,(l/\delta_{th})^{-1/2}$ numbers away from the wall. These u'/S_L and l/δ_{th} values are representative of the thin reaction zones regime of premixed turbulent combustion [62]. The maximum value of non-dimensional grid spacing $x^+ = \Delta x\sqrt{\tau_w/\rho}\,/\nu$ (where τ_w is the wall shear stress and ν is the kinematic viscosity) remains smaller than unity during the course of simulation for all cases considered here. Each simulation has been conducted for $t \geq 12\delta_Z/S_L$ when the minimum, maximum and mean value of wall heat fluxes reach similar values after flame quenching [11]. For cases A-E, $12\delta_Z/S_L$ is equivalent to 21, 30, 21, 15 and 21 initial eddy turn-over times, respectively. The DNS data were ensemble averaged on the transverse plane (i.e. x_2 and x_3) at a given x_1 −location to evaluate the Favre/Reynolds averaged quantities.

3. RESULTS AND DISCUSSION

3.1. Flame turbulence interaction and vorticity distribution

The instantaneous distribution of $\sqrt{\omega_i\omega_i} \times \delta_Z/S_L$ in the central $x_1 - x_2$ plane for case E, along with c contours ranging from 0.1 to 0.9 (bottom to top), are presented in Fig. 1. As discussed in detail elsewhere [11,17,31, 35-52], the imbalance between conductive heat flux and mass diffusive flux leads to simultaneous occurrence of high temperature and reactant concentration in positively stretched regions for flames with $Le < 1$ due to strong (weak) focusing (defocusing) of species (heat). This leads to higher extents of flame wrinkling and burning rate for the flames with $Le < 1$ than the corresponding $Le = 1.0$ flames, when combustion takes place away from the wall. Just the opposite mechanism is responsible for smaller extent of wrinkling and burning rate for the $Le > 1$ flames than in the corresponding $Le = 1.0$ flame when the flame is away from the wall. Therefore the flame wrinkles reach close to the wall and eventually quench at an earlier time instant for smaller Le.

Furthermore, the extent of flame wrinkling increases with increasing turbulence intensity u'/S_L when the flame is away from the wall, and thus the flame wrinkles reach close to the wall and quench at an earlier time instant for higher u'/S_L (not shown here, but refer to Table 2 of Ref. [11] for supporting evidence). Accordingly, smaller values of flame surface area and burning rate are obtained at an advanced stage of flame quenching for smaller (higher) Le (u'/S_L) because quenching initiates at an earlier time for these flames (e.g. quenching starts at about $t \approx 4.5\delta_Z/S_L$ ($t \approx 1.7\delta_Z/S_L$) for case A (case E) for this configuration) [11]. This can be substantiated from the temporal evolutions of the flame surface area and volume-integrated chemical reaction rate presented in Table 2 in Ref. [11].

Figure 1 shows that large magnitudes of $\sqrt{\omega_i\omega_i} \times \delta_Z/S_L$ are concentrated on the unburned gas side of the flame and $\sqrt{\omega_i\omega_i} \times \delta_Z/S_L$ decreases significantly across the flame for all Le cases. This can be supported by Fig. 2 where the variations of $\overline{(\omega_\iota\omega_\iota)^{1/2}}$ and scaled-up mean rate of product creation $\bar{\dot{\omega}}_c$ with x_1/δ_Z are shown for cases A, C and E. Cases B and D are qualitatively similar to cases A and E respectively and thus are not shown in Fig. 2 and subsequent figures. Figure 2 shows that $\overline{(\omega_\iota\omega_\iota)^{1/2}}$ attains its highest value at the wall and gradually decays from unburned to burned gas side of the flame-brush, besides it is consistent with previous findings [29,30], which also reported a decrease in the magnitude of vorticity within flame brush. The physical explanation for the decay of vorticity magnitude across the flame brush will be discussed later in this paper by analysing the statistical behaviours of vorticity and enstrophy transport (see subsection 3.4). The background colour in Fig. 2-10 indicates the Favre-averaged value of $\tilde{c}$, which illustrates the flame position at the corresponding time instants.

A comparison between $\overline{(\omega_\iota\omega_\iota)^{1/2}}$ and $\bar{\dot{\omega}}_c$ distributions reveals that before quenching $\overline{(\omega_\iota\omega_\iota)^{1/2}}$ attains high magnitudes in the cases with high (small) u'/S_L (Le) (e.g. see the top right plot (case E, $Le = 0.8$, and $t = 2\,\delta_Z/S_L$)). A comparison between spatial profiles of $\bar{\dot{\omega}}$, obtained in the five cases at $t = 2\,\delta_Z/S_L$, indicates that the mean flame brush thickness is significantly increased by u'/S_L from case A to case E. As a result, the leading (trailing) edge of the flame brush is more close to (far from) the wall in case E when compared to case A. This difference in the x_1-coordinates of flame-brush edges is of substantial importance for analysing results obtained at the time instant $t = 2\,\delta_Z/S_L$ because the flame in case E is closer to the wall (than in case A) before flame quenching.

Figure 2 shows also that the mean chemical reaction rate drops significantly in a region given by $x_1/\delta_Z < (Pe_{min})_L$ where $(Pe_{min})_L$ is the minimum Peclet number for HOQ of laminar flames, $Pe = X/\delta_Z$ and X is the wall normal distance of the $(\hat{T} - T_0)/(T_{ad} - T_0) = 0.9$ isosurface [3,9]. Thus, $(Pe_{min})_L$ can be considered as the normalised laminar quenching distance because chemical reaction cannot be sustained in the region given by $x_1/\delta_Z < (Pe_{min})_L$ due to low temperature as a result of heat loss through the wall. It has been found that $(Pe_{min})_L = 3.09$, 2.83 and 2.75 for $Le = 0.8$, 1.0 and 1.2 respectively. These values are in agreement with previous computational [3] and experimental [56-58] findings. In the $Le = 0.8$ case, the mean reaction rate $\bar{\dot{\omega}}_c$ attains non-zero values for $x_1/\delta_Z < (Pe_{min})_L$ because the minimum Peclet number for turbulent $Le = 0.8$ flames remains smaller than the laminar value [11], whereas the minimum Peclet number for laminar and turbulent flames remain almost the same for $Le = 1.0$ and 1.2. Interrested readers are referred to Ref. [11] for further discussion on the minimum Peclet number and its Lewis number dependence.

3.2. Statistical behaviour of the magnitude of vorticity components

The variations of the rms values of the normalised Favre-averaged vorticity magnitude $\left[\overline{\rho(\omega_\iota - \widetilde{\omega}_\iota)^2}/\bar{\rho}\right]^{1/2} \times \delta_Z/S_L$ and its components (i.e. $\left[\overline{\rho(\omega_1 - \widetilde{\omega}_1)^2}/\bar{\rho}\right]^{1/2}$, $\left[\overline{\rho(\omega_2 - \widetilde{\omega}_2)^2}/\bar{\rho}\right]^{1/2}$ and $\left[\overline{\rho(\omega_3 - \widetilde{\omega}_3)^2}/\bar{\rho}\right]^{1/2}$) with x_1/δ_Z are shown for cases A, C and E in Fig. 3. A difference between $\left[\overline{\rho(\omega_1 - \widetilde{\omega}_1)^2}/\bar{\rho}\right]^{1/2}$ and $\left[\overline{\rho(\omega_2 - \widetilde{\omega}_2)^2}/\bar{\rho}\right]^{1/2}$ (or $\left[\overline{\rho(\omega_3 - \widetilde{\omega}_3)^2}/\bar{\rho}\right]^{1/2}$) has been found before the flame interacts with the wall (cf. violet, red and blue lines in the top right plot). The presence of the flame significantly modifies the initial isotropic vorticity field, and it is consistent with previous analyses [16,29-31] which reported substantial anisotropy between the vorticity components due to baroclinic torque contribution. The extent of this anisotropicity increases with decreasing (increasing) Le (u'/S_L) when the flame is away from the wall, and this anisotropic behaviour is particularly strong in the near-wall region. The component $\left[\overline{\rho(\omega_1 - \widetilde{\omega}_1)^2}/\bar{\rho}\right]^{1/2}$ decays to close to the wall, whereas $\left[\overline{\rho(\omega_2 - \widetilde{\omega}_2)^2}/\bar{\rho}\right]^{1/2}$ and $\left[\overline{\rho(\omega_3 - \widetilde{\omega}_3)^2}/\bar{\rho}\right]^{1/2}$ increase significantly in the near-wall region. Figure 3 indicates that $\left[\overline{\rho(\omega_2 - \widetilde{\omega}_2)^2}/\bar{\rho}\right]^{1/2}$ and $\left[\overline{\rho(\omega_3 - \widetilde{\omega}_3)^2}/\bar{\rho}\right]^{1/2}$ are principally responsible for the rise of $\left[\overline{\rho(\omega_\iota - \widetilde{\omega}_\iota)^2}/\bar{\rho}\right]^{1/2}$ in the near-wall region.

3.3. Statistical behaviour of vorticity transport

It is necessary to analyse the statistical behaviour of the terms of Eq. 1 to explain the near-wall behaviour of $\overline{(\omega_\iota\omega_\iota)^{1/2}}$ and $\left[\overline{\rho(\omega_\iota - \widetilde{\omega}_\iota)^2}/\bar{\rho}\right]^{1/2}$, and the observed anisotropy of their components. The variations of $\overline{(t_{1t}t_{1t})^{1/2}}$, $\overline{(t_{21t}t_{21t})^{1/2}}$, $\overline{(t_{22t}t_{22t})^{1/2}}$, $\overline{(t_{3t}t_{3t})^{1/2}}$ and $\overline{(t_{4t}t_{4t})^{1/2}}$ with x_1/δ_Z are shown in Fig. 4 for cases A, C and E, where $\overline{\left(t_{qt}t_{qt}\right)^{1/2}} = \overline{[(\delta_{\iota J} - n_\iota n_J)t_{q\iota}t_{qJ}]^{1/2}}$ with $q = 1, 21, 22, 3, 4$ and $\vec{n}$ is the normal vector pointing outward on the wall (i.e. positive x_1-direction for this configuration). The corresponding variations of $\overline{(t_{1n}t_{1n})^{1/2}}$, $\overline{(t_{21n}t_{21n})^{1/2}}$, $\overline{(t_{22n}t_{22n})^{1/2}}$, $\overline{(t_{3n}t_{3n})^{1/2}}$ and $\overline{(t_{4n}t_{4n})^{1/2}}$ with x_1/δ_Z are shown

in Fig. 5 where $\overline{(t_{qn}t_{qn})^{1/2}} = \overline{[(n_\iota n_J)t_{q\iota}t_{qJ}]^{1/2}}$ with $q = 1, 21, 22, 3, 4$. It is important to note that three time instants $t_1 = 2\delta_Z/S_L$, $t_2 = 6\delta_Z/S_L$ and $t_3 = 10\delta_Z/S_L$ are shown in Figs. 4 and 5. The flame quenching has started at these time instants for all cases but they are at different stages of flame quenching. The cases with higher u'/S_L propagates faster and starts to interact with the wall at an earlier time instant. Similarly, the cases with smaller values of Le propagate faster towards the wall and thus the effects of flame quenching set in at an earlier time instant in these cases. Thus, the effects of flame quenching will be most prominent in case E and least pronounced in case A. Please refer to the temporal evolutions of wall heat flux and wall Peclet number in Fig. 1 and Table 2 of Lai and Chakraborty [11] and the associated discussion for further information on this aspect.

Figures 4 and 5 indicate that the magnitudes of all the terms shown in these figures increase with decreasing (increasing) Le (u'/S_L). The contributions of the vortex-stretching and the combined molecular diffusion and dissipation (i.e. $\overline{(t_{1n}t_{1n})^{1/2}}$ or $\overline{(t_{1t}t_{1t})^{1/2}}$ and $\overline{(t_{22n}t_{22n})^{1/2}}$ or $\overline{(t_{22t}t_{22t})^{1/2}}$) are of substantial importance in the vorticity transport for all cases when the flame is away from the wall. However, the magnitudes of $\overline{(t_{1n}t_{1n})^{1/2}}$, $\overline{(t_{1t}t_{1t})^{1/2}}$ and $\overline{(t_{22n}t_{22n})^{1/2}}$ decrease as the wall is approached by the flame (see black solid lines associated with different instants in Figs. 4 and 5 or red dashed lines in Fig. 5). At each instant, the magnitude of $\overline{(t_{22t}t_{22t})^{1/2}}$ increases significantly in the near-wall region (see red dashed lines in Fig. 4). The strong vorticity diffusion at the wall and high values of vorticity gradient magnitude, along with the gradient of dilatation rate, are responsible for the rise of the magnitude of the term $\overrightarrow{t_{22}} = (\mu/\rho)\nabla^2\vec{\omega} + (\mu/3\rho)\nabla \times \nabla(\nabla.\vec{u})$ in transverse directions in the near-wall region. At large u'/S_L (case E), the magnitude of baroclinic torque term $\overrightarrow{t_4}$ becomes comparable to the combined molecular diffusion and dissipation term (i.e. $\overrightarrow{t_{22}}$) in the near-wall

region, see red dashed and blue solid lines. This effect becomes increasingly pronounced with decreasing Le.

A comparison between Figs. 4 and 5 reveals that $\overline{(t_{4t}t_{4t})^{1/2}}$ remains greater than $\overline{(t_{4n}t_{4n})^{1/2}}$ in the flame-brush region before flame quenching for cases C and E but this effect is relatively less pronounced for case A. Figure 5 shows that $\overline{(t_{4n}t_{4n})^{1/2}}$ becomes one of the dominant terms as the flame starts to interact with the wall. For low Mach number $Le = 1.0$ flames c can be equated to non-dimensional temperature $T = (\hat{T} - T_0)/(T_{ad} - T_0)$ when the flame is away from the wall and thus $\nabla\rho = \nabla\{\rho_0/(1 + \tau T)\}$ can be equated to $\nabla\rho = -\tau\rho^2\nabla c/\rho_0 = \tau\rho^2|\nabla c|\vec{N}/\rho_0$ (where $\vec{N} = -\nabla c/|\nabla c|$ is the local flame normal vector [29]), which implies $\nabla\rho$ and ∇c are parallel to each other when the flame is away from the wall. As the flame normal vector $\vec{N}$ and the unit normal vector $\vec{n}$ outward on the wall mostly aligned with each other in the case of HOQ of statistically planar flames (not shown here), $\overline{(t_{4n}t_{4n})^{1/2}}$ is negligible when the flame is away from the wall in the $Le = 1.0$ case. However, $c \neq T$ in the near-wall region even for $Le = 1.0$ [11] and this non-equality holds both away from and near to the wall for flames with $Le \neq 1.0$. When a flame is close to the wall, the misalignment between $\nabla\rho$ and ∇c (or ∇T and ∇c) in the near-wall region leads to a rise in $\overline{(t_{4n}t_{4n})^{1/2}}$. The misalignment of $\nabla\rho$ and ∇c leads to a non-negligible magnitude of $\overline{(t_{4n}t_{4n})^{1/2}}$ within a flame even when the flame is away from wall for $Le \neq 1.0$, with the magnitude of $\overline{(t_{4n}t_{4n})^{1/2}}$ rising in the near-wall region due to increased misalignment between $\nabla\rho$ and ∇c . Figures 4 and 5 suggest that the baroclinic terms are principally responsible for the anisotropy between the vorticity components. It is important to note that flame quenching gives rise to high temperature gradient close to the wall , which in turn leads to considerable density gradient in the near wall region (not shown here), and thus the baroclinic torque contribution assumes significant values at the

wall. The baroclinic torque contribution $\overline{(t_{4t}t_{4t})^{1/2}}$ to the evolution of the vorticity field near the wall is weakest in case A. It is shown elsewhere (see Figs. 2, 3 and 7 in Ref. [11]) that the flame quenching initiates at an earlier time instant for higher values of u'/S_L. Thus, at a given instant, case A is associated with an earlier stage of quenching in comparison to cases C and E, because the weakly turbulent case A propagates at a slower rate towards the wall than cases C and E. This effect is manifested in the near-wall behaviour of the baroclinic torque contribution $\overline{(t_{4t}t_{4t})^{1/2}}$ in Fig. 4 which shows that the magnitude of $\overline{(t_{4t}t_{4t})^{1/2}}$ close to the wall is smaller in case A than in cases C and E due to relatively smaller extent of flame-wall interaction in this case in comparison to the other cases.

The dilatation contributions $\overline{(t_{3n}t_{3n})^{1/2}}$ and $\overline{(t_{3t}t_{3t})^{1/2}}$ (see violet lines in Figs. 4 and 5) exhibit significant magnitudes within the flame-brush but they become negligible on burned gas sides, because the density is almost constant during the quenching event (or exactly constant when the flame is far from the wall). However, the terms $\overline{(t_{3n}t_{3n})^{1/2}}$ and $\overline{(t_{3t}t_{3t})^{1/2}}$ are significant in the burned gas in the near-wall region even after the quenching is initiated. There is a considerable amount of density variation in the near-wall region due to sharp change in temperature even after the flame is quenched, which gives rise to significant values of dilatation rate $\nabla \cdot \vec{u}$ and the dilatation contributions $\overline{(t_{3n}t_{3n})^{1/2}}$ and $\overline{(t_{3t}t_{3t})^{1/2}}$. However, $\overline{(t_{3n}t_{3n})^{1/2}}$ and $\overline{(t_{3t}t_{3t})^{1/2}}$ eventually decay with the decay in vorticity magnitude.

The contributions $\overline{(t_{21n}t_{21n})^{1/2}}$ and $\overline{(t_{21t}t_{21t})^{1/2}}$ are significant within the flame-brush (where the density variation is significant) before flame quenching, and their magnitudes increase near the wall due to non-zero $\nabla\rho$ and high values of $\partial\tau_{kl}/\partial x_l$ induced by the wall.

3.4. Statistical behaviour of the enstrophy transport

The variations of $T_I, T_{II}, T_{III}, T_{IV}$ and T_V with x_1/δ_Z are reported in Figs. 6 and 7 for cases A and E respectively (a monotonic qualitative trend is observed from case A to case E). Figures 6 and 7 shows that the magnitudes of these terms increase significantly with decreasing (increasing) Le (u'/S_L). The vortex-stretching term T_I remains positive throughout the flame-brush for all cases away from wall, but negative values of T_I have been found in the near-wall region. The vortex-stretching term T_I can be expressed as: $T_I = \overline{2\Omega(e_\alpha \cos^2\theta_\alpha + e_\beta \cos^2\theta_\beta + e_\gamma \cos^2\theta_\gamma)}$ [17,31], where e_α, e_β and e_γ are the most extensive (i.e. positive), intermediate, and the most compressive (i.e. negative) principal strain rates, and $\theta_\alpha, \theta_\beta$ and θ_γ are the angles between $\vec{\omega}$, and the eigenvectors associated with the eigenvalues e_α, e_β and e_γ respectively. A negative contribution of T_I suggests a weak (strong) alignment of $\vec{\omega}$ with e_α (e_γ) in the near-wall region. The extent of $\vec{\omega}$ alignment with the principal strain rate e_i can be quantified from the values of $\Psi_i = |\cos\theta_i|$ (where $i = \alpha, \beta$ and γ) and Ψ_i is equal to 1.0 (0.0) for collinear (perpendicular) alignment between $\vec{\omega}$ and the eigenvector corresponding to e_i. Accordingly, a collinear alignment of $\vec{\omega}$ with e_α (e_γ) leads to a positive (negative) value of $T_I = \overline{2\Omega(e_\alpha \cos^2\theta_\alpha + e_\beta \cos^2\theta_\beta + e_\gamma \cos^2\theta_\gamma)}$ [17,31]. The variations of $\overline{\Psi_\alpha}, \overline{\Psi_\beta}$ and $\overline{\Psi_\gamma}$ with x_1/δ_Z for cases A, C and E are reported in Fig. 8, which demonstrates that $\overline{\Psi_\beta}$ has a magnitude which is either greater than or comparable to $\overline{\Psi_\alpha}$ and $\overline{\Psi_\gamma}$. Thus, it suggests a predominant alignment of $\vec{\omega}$ with the eigenvector associated with intermediate strain rate e_β, and this is consistent with previous findings [13-28], which demonstrated that the vorticity vector aligns with the intermediate principal strain rate e_β in turbulent non-reacting and reacting flows regardless of the regime of combustion, heat release parameter and Lewis number. Furthermore, Fig. 8 shows that the alignment of $\vec{\omega}$ with e_α (i.e. in other words the magnitude of $\overline{\Psi_\alpha}$) decreases in the regions where the effects of heat release are weak, which is also consistent with previous observations [14-17]. The extent of alignment of $\vec{\omega}$ with e_γ also

decreases on the unburned gas side of the flame brush. It can be seen from Fig. 8 that both $\overline{\Psi_\beta}$ and $\overline{\Psi_\gamma}$ assume greater magnitudes than $\overline{\Psi_\alpha}$ as the flame approaches the wall. This leads to negative values of T_I in the near-wall region.

Figures 6 and 7 show that the magnitude of viscous torque term T_{II} remains small in comparison to the other terms when the flame is away from the wall, but it becomes a dominant sink in the near-wall region when the flame approaches the wall.

The term T_{III} remains negative away from the wall for all cases but it becomes positive for $x_1/\delta_Z < (Pe_{min})_L$. Substituting $\tau_{kl} = \mu(\partial u_k/\partial x_l + \partial u_k/\partial x_l) - 2(\mu/3)\delta_{kl}(\partial u_m/\partial x_m)$ in $T_{III} = \overline{\epsilon_{ijk}\omega_i/\rho\,(\partial^2\tau_{kl}/\partial x_j\partial x_l)}$ leads to [31]: $T_{III} = \overline{(\mu/\rho)\nabla^2\Omega} + \overline{(\mu/3\rho)\vec{\omega}\cdot[\nabla\times\nabla(\nabla\cdot\vec{u})]} + f(\mu) - D_v$ where $f(\mu)$ represents the contributions from viscosity gradients and $-D_v = -\overline{(\mu/\rho)(\partial\omega_\iota/\partial x_l)(\partial\omega_\iota/\partial x_l)}$ is the molecular dissipation of enstrophy. The variations of $\overline{(\mu/\rho)\nabla^2\Omega}$, $\overline{(\mu/3\rho)\vec{\omega}\cdot[\nabla\times\nabla(\nabla\cdot\vec{u})]}$ and $(-D_v)$ with x_1/δ_Z are reported in Figs. 9 and 10 for cases A and E respectively (a monotonic qualitative trend is observed from case A to case E). The term $f(\mu)$ is identically zero for the cases considered here (i.e. $\mu = \text{constant}$) and thus is not shown in Figs. 9 and 10. It can be seen from Figs. 9 and 10 that the magnitude of $\overline{(\mu/\rho)\nabla^2\Omega}$ remains negligible in comparison to that of $\overline{(\mu/3\rho)\vec{\omega}\cdot[\nabla\times\nabla(\nabla\cdot\vec{u})]}$ and $(-D_v)$. Away from the wall, and the term T_{III} is negative principally due to $(-D_v)$. On the contrary, in the near-wall region, the contribution of $\overline{(\mu/3\rho)\vec{\omega}\cdot[\nabla\times\nabla(\nabla\cdot\vec{u})]}$ overwhelms the sink contribution of $(-D_v)$, and yields a positive value of T_{III}.

The dilatation term T_{IV} is negative, and plays an important role only within the flame-brush away from the wall. The baroclinic torque term T_V remains positive, but vanishes outside the flame-brush when the flame is away from the wall. Moreover, this term can exhibit negative values of T_V in the near-wall region during flame quenching (note that flame quenching for case E starts at $t < 2\delta_Z/S_L$). At the last stage of flame-wall interaction, e.g. at $t = 10\delta_Z/S_L$ in case E, see Fig. 7, both the baroclinic torque term T_{IV} and the molecular diffusion and disspation term T_{III} play significant roles in the near-wall region, see left columns in Fig. 7, for all Lewis number cases considered here.

Equation 2 can be rewritten as [30,31]:

$$\overline{D}\,\overline{\Omega}/\overline{D}t = T_I + T_{II} + T_{III} + T_{IV} + T_V - \overline{u'_k\,\partial\Omega'/\partial x_k} \qquad (3)$$

where $\overline{D}(\ )/\overline{D}t = \partial(\ )/\partial t + \bar{u}_k\,\partial(\ )/\partial x_k$ is the material derivative associated with the mean flow. Although $T_{VI} = -\overline{u'_k\,\partial\Omega'/\partial x_k}$ (see blue dashed lines in Figs. 6 and 7) exhibits local positive (negative) values in cases A and B (cases C-E), $\overline{D}\,\overline{\Omega}/\overline{D}t$ remains predominantly negative (see black dashed lines), but is positive in the near-wall region (i.e. $x_1/\delta_Z < (Pe_{min})_L$) at early times for small values of u'/S_L (e.g. case A). A predominantly negative value of $\overline{D}\,\overline{\Omega}/\overline{D}t$ for the major part of the flame-brush is consistent with the decay of $\overline{(\omega_\iota\omega_\iota)^{1/2}} \times \delta_{th}/S_L$ from unburned to burned gas side of the flame-brush (see Fig. 2). As the quenching progresses $\overline{D}\,\overline{\Omega}/\overline{D}t$ shows more likelihood of exhibiting negative values close to the wall, which acts to reduce $\overline{(\omega_\iota\omega_\iota)^{1/2}}$ in the near-wall region.

4. CONCLUSIONS

The statistical behaviour of vorticity and enstrophy transport in HOQ of statistically planar turbulent premixed flames by an isothermal inert wall has been analysed using DNS data for

different values of Da, Ka and Le. In all cases the vorticity magnitude $\sqrt{\omega_i\omega_i}$ drops from the unburned side (which is in contact with the wall) to the burned gas side of the flame-brush and the highest magnitude of $\sqrt{\omega_i\omega_i}$ is obtained at the wall. Furthermore, both $\sqrt{\omega_i\omega_i}$ and the magnitudes of the terms of the vorticity transport equation increase with decreasing (increasing) Le (u'/S_L). The presence of the flame and wall induce significant amount of anisotropy between vorticity components, and the baroclinic torque has been shown to be principally responsible for this anisotropic behaviour. The vortex-stretching and viscous dissipation terms have been found to be the significant contributors to the enstrophy transport for all cases when the flame is away from the wall. As the flame approaches the wall, the baroclinic torque begins to play increasingly important roles in the enstrophy transport. Furthermore, combined molecular diffusion and dissipation contribution remains negative away from the wall but becomes positive near the wall due to the torque arising from dilatation rate gradient, caused by the local temperature and density variations. Further analysis using experimental and detailed chemistry DNS data at high values of turbulent Reynolds number Re_t will be necessary for more comprehensive understanding.

ACKNOWLEDGEMENTS

The authors are grateful to EPSRC and N8/ARCHER for the financial and computational support. The third author (AL) was supported by the Chalmers Combustion Research Centre (CERC).

REFERENCES

1. P.A. Durbin, B.A. Pettersson Reif, Statistical Theory and Modelling for Turbulent Flames, Willey, 2010.

2. S.B. Pope, Turbulent Flow, Cambridge University Press, Cambridge, UK, 2000.

3. T.J. Poinsot, D.C. Haworth, G. Bruneaux, Numerical simulations of Lewis number effects in turbulent premixed flames**,** Combust. Flame 95 (1993) 118-132.

4. G. Bruneaux, K. Akselvoll, T. Poinsot, J.H. Ferziger, Flame-wall interaction simulations in a turbulent channel flow, Combust. Flame. 107 (1996) 27-36.

5. G. Bruneaux, T. Poinsot, J. H. Ferziger, Premixed flame-wall interaction in a turbulent channel flow: budget for the flame surface density evolution equation and modelling, J. Fluid Mech. 349 (1997) 191-219.

6. T. Alshaalan, C. J. Rutland, Turbulence, scalar transport, and reaction rates in flame-wall interaction, Proc. Combust. Inst. 27 (1998) 793-799.

7. T. Alshaalan, C. J. Rutland, Wall heat flux in turbulent premixed reacting flow, Combust. Sci Technol. 174 (2002) 135-165.

8. B. Boust, J. Sotton, S.A. Labuda, M. Bellenoue, Thermal formulation for single-wall quenching of transient laminar flames, Combust. Flame 149 (2007) 286-294.

9. A. Gruber, R. Sankaran, E.R. Hawkes, J.H. Chen, Turbulent flame-wall interaction: a direct numerical simulation study, J. Fluid. Mech. 658 (2010) 5-32.

10. A. Gruber, J.H. Chen, D. Valiev, C.K. Law, Direct numerical simulation of premixed flame boundary layer flashback in turbulent channel flow, J. Fluid. Mech.709 (2012) 516-542.

11. J. Lai, N. Chakraborty, Effects of Lewis Number on head on quenching of turbulent premixed flames: a direct numerical simulation analysis, Flow, Turb. Combust. 96 (2016) 279-308.

12. A.N. Lipatnikov, J. Chomiak, Effects of premixed flames on turbulence and turbulent scalar transport, Prog. Energy Combust. Sci. 36 (2010) 1-102.

13. K.K. Nomura, S.E. Elghobashi, The structure of inhomogeneous turbulence in variable density nonpremixed flames, Theor. Fluid Dyn. 5 (1993) 153-175.

14. O.N. Boratov, S.E. Elghobashi, R. Zhong, Characteristics of chemically reacting compressible homogeneous turbulence, Phys. Fluids 10 (1996) 2260-2267.

15. F.A. Jaberi, D. Livescu, C.K. Madnia, Characteristics of chemically reacting compressible homogeneous turbulence, Phys. Fluids, 12 (2000) 1189-1209.

16. P.E. Hamlington, A.Y. Poludnenko, E.S. Oran, Interactions between turbulence and flames in premixed reacting flows, Phys. Fluids. 23 (2011) 125111.

17. N. Chakraborty, Statistics of vorticity alignment with local strain rates in turbulent premixed flames, Eur. J. Mech. B/Fluids 46 (2014) 201-220.

18. A. Tsinober, L. Shtilman, H. Vaisburd, A study of properties of vortex stretching and enstrophy generation in numerical and laboratory turbulence, Fluid Dyn. Research, 21 (1997) 477-494.

19. E.D. Siggia, Numerical study of small scale intermittency in three-dimensional turbulence, J. Fluid Mech. 107 (1981) 375-406.

20. W.T. Ashurst, A. Kerstein, R. M. Kerr, C.H. Gibson, Alignment of vorticity and scalar gradient with strain rate in simulated Navier–Stokes turbulence, Phys. Fluids A, 30 (1987) 2343-2354.

21. Z.-S. She, E. Jackson, S. Orszag, Structure and dynamics of homogeneous turbulence: models and simulations, Proc. Roy. Soc. A, 434 (1991) 101-124.

22. A. J. Majda, Vorticity, turbulence, and acoustics in fluid flow, SIAM Rev.33 (1991) 349-388.

23. J. Jimenez, Kinematic alignment effects in turbulent flows, Phys. Fluids A 4 (1992) 652-654.

24. A. Tsinober , E. Kit, T. Dracos, Experimental investigation of the field of velocity gradients in turbulent flows, J. Fluid Mech. 242 (1992) 169-192.

25. B.W. Zeff, D.D. Lanterman, R. McAllister, R. Roy, E.J. Kostelich, D.P. Lathrop, Measuring intense rotation and dissipation in turbulent flows, Nature 421 (2003) 146-149.

26. B. Lüthi, A. Tsinober , W. Kinzelbach, Lagrangian measurement of vorticity dynamics in turbulent flow, J. Fluid Mech. 528 (2005) 87-118.

27. P.E. Hamlington, J. Schumacher, W.J.A. Dahm, Local and nonlocal strain rate and vorticity alignment in turbulent flows, Phys. Rev. E. 77 (2008) 026303.

28. A. Tsinober, Vortex stretching versus production of strain/dissipation, Isaac Newton Inst. Report, 2009.

29. T.C. Treurniet, F.T.M. Nieuwstadt, B.J. Boersma, Direct numerical simulation of homogeneous turbulence in combination with premixed combustion at low Mach number modelled by the G-equation, J. Fluid Mech. 565 (2006) 25-62.

30. A.N. Lipatnikov, S. Nishiki, T. Hasegawa, A direct numerical study of vorticity transformation in weakly turbulent premixed flames, Phys. Fluids 26 (2014) 105104.

31. N. Chakraborty, I. Konstantinou, A. Lipatnikov, Effects of Lewis number on vorticity and enstrophy transport in turbulent premixed flames, Phys. Fluids 28 (2016) 015109.

32. H. Tennekes, J.L. Lumley, A first course in turbulence, MIT press, Massachusetts, USA, 1972.

33. T. Poinsot, T. Echekki, M. Mungal, A study of the laminar flame tip and implications for turbulent premixed combustion, Combust. Sci. Technol., 81(1-3) (1992) 45-57.

34. D.S. Louch, K.N.C. Bray, Vorticity in unsteady premixed flames: Vortex pair-premixed flame interactions under imposed body forces and various degrees of heat release and laminar flame thickness, Combust. Flame, 125 (2001) 1279-1309.

35. G.I. Sivashinsky, Diffusional-thermal theory of cellular flames, Combust. Sci. Technol. 16 (1977) 137-146.

36. P. Clavin, F.A. Williams, Effects of molecular diffusion and thermal expansion on the structure and dynamics of turbulent premixed flames in turbulent flows of large scale and small intensity, J. Fluid Mech. 128 (1982) 251-282.

37. P. Pelce, P. Clavin, Influence of hydrodynamics and diffusion upon the stability limits of laminar premixed flames, J. Fluid Mech. 124 (1982) 219-237.

38. D.C. Haworth, T.J. Poinsot, Numerical simulations of Lewis number effects in turbulent premixed flames, J. Fluid Mech. 244 (1992) 405-436.

39. C. Rutland, A. Trouvé, Direct simulations of premixed turbulent flames with nonunity Lewis numbers, Combust. Flame 94 (1993) 41-57.

40. A. Trouvé, T. Poinsot, The evolution equation for flame surface density in turbulent premixed combustion, J. Fluid Mech. 278 (1994) 1-31.

41. N. Chakraborty, R.S. Cant, Influence of Lewis Number on curvature effects in turbulent premixed flame propagation in the thin reaction zones regime, Phys. Fluids 17 (2005) 105105.

42. J. Yuan, Y. Ju, C.K. Law, Coupled hydrodynamic and diffusional-thermal instabilities in flame propagation at small Lewis numbers, Phys. Fluids 17 (2005) 074106.

43. N. Chakraborty, R.S. Cant, Influence of Lewis number on strain rate effects in turbulent premixed flame propagation in the thin reaction zones regime, Int. J. Heat Mass Trans. 49 (2006) 2158-2172.

44. N. Chakraborty, M. Klein, Influence of Lewis number on the surface density function transport in the thin reaction zones regime for turbulent premixed flames, Phys. Fluids, 20 (2008) 065102.

45. N. Chakraborty, R.S. Cant, Effects of Lewis number on scalar transport in turbulent premixed flames, Phys. Fluids, 21 (2009) 035110.

46. N. Chakraborty, M. Katragadda, R.S. Cant, Effects of Lewis number on turbulent kinetic energy transport in turbulent premixed combustion, Phys. Fluids, 23 (2011) 075109.

47. N. Chakraborty, M. Katragadda, R.S. Cant, Statistics and modelling of turbulent kinetic energy transport in different regimes of premixed combustion, Flow Turb. Combust., 87 (2011) 205-235.

48. I. Han, K.Y. Huh, Roles of displacement speed on evolution of flame surface density for different turbulent intensities and Lewis numbers in turbulent premixed combustion, Combust. Flame 152 (2008) 1409-1417.

49. N. Chakraborty, M. Klein, N. Swaminathan, Effects of Lewis number on the reactive scalar gradient alignment with local strain rate in turbulent premixed flames, Proc. Combust. Inst., 32 (2009) 085108.

50. N. Chakraborty, N. Swaminathan, Effects of Lewis number on scalar dissipation transport and its modelling implications for turbulent premixed combustion, Combust. Sci. Technol.182 (2010) 1201-1240.

51. N. Chakraborty, N. Swaminathan, Effects of Lewis number on scalar variance transport in turbulent premixed flames, Flow Turb. Combust. 87 (2011) 261-292.

52. N. Chakraborty, A.N. Lipatnikov, Effects of Lewis number on the statistics of conditional fluid velocity in turbulent premixed combustion in the context of Reynolds Averaged Navier Stokes simulations, Phys. Fluids 25 (2013) 045101.

53. J.H. Chen, A. Choudhary, M. de Supinski, B. de Vries, E.R. Hawkes, S. Klasky, W.K. Liao, K.L. Ma, J. Mellor-Crummey, N. Podhorski, R. Sankaran, S. Shende, S. and C.S. Yoo, Terascale direct numerical simulations of turbulent combustion using S3D. *Comput. Sci. Discov.*, **2** (2009) 015001.

54. N. Chakraborty, R.S. Cant, Unsteady effects of strain rate and curvature on turbulent premixed flames in an inflow-outflow configuration, *Combust. Flame*, 137 (2004) 129-147.

55. N. Chakraborty, E.R. Hawkes, J.H. Chen, R.S. Cant, Effects of strain rate and curvature on Surface Density Function transport in turbulent premixed CH_4-air and H_2-air flames: A comparative study, *Combust. Flame*, 154 (2008) 259-280.

56. S.R.Vosen, R. Greif, C. Westbrook, Unsteady heat transfer in laminar flame quenching , Proc. Combust. Inst. 20 (1984) 76-83.

57. J. Jarosinsky, A survey of recent studies on flame extinction, Heat transfer during laminar flame quenching, Combust. Sci. Technol. 12 (1986) 81-116.

58. W.M. Huang, S.R. Vosen, R. Greif, Heat transfer during laminar flame quenching, Proc. Combust. Inst. 21 (1986) 1853-1860.

59. T. Poinsot, S.K. Lele, Boundary conditions for direct simulation of compressible viscous flows, J. Comp. Phys. 101 (1992) 104-129.

60. R.S. Rogallo, Numerical experiments in homogeneous turbulence, NASA Technical Memorandum 81315, NASA Ames Research Center, California, 1981.

61. G. K. Bachelor, A.A. Townsend, Decay of turbulence in final period, Proc. R. Soc. London A194 (1948) 527-543.

62. N. Peters, Turbulent Combustion, Cambridge University Press, Cambridge, UK, 2000.

TABLES

Case	u'/S_L	l/δ_{th}	Da	Ka
A	5.0	1.67	0.33	8.67
B	6.25	1.44	0.23	13.0
C	7.5	2.50	0.33	13.0
D	9.0	4.31	0.48	13.0
E	11.25	3.75	0.33	19.5

Table 1: List of initial simulation parameters away from the wall.

FIGURE CAPTIONS

Fig. 1: Distribution of $(\omega_i\omega_i)^{1/2} \times \delta_Z/S_L$ and c (white line from 0.1 to 0.9 with step of 0.2 from bottom to top) fields on $x_1 - x_2$ mid plane for turbulent case E with $Le = 0.8$, 1.0 and 1.2 at $t = 1, 2$ and 4 δ_Z/S_L.

Fig. 2: Variation of $\overline{(\omega_i\omega_i)^{1/2}} \times \delta_Z/S_L$ (——), $15 \times \bar{\omega}_c \times \delta_Z/\rho_0 S_L$ (——) and $\tilde{c}$ with x_1/δ_Z for cases A, C and E at $t = 2\,\delta_z/S_L$, $6\,\delta_z/S_L$ and $10\,\delta_z/S_L$ (1st-3rd row). For illustration purpose $\tilde{c}$ is indicated by background colour and the vertical dotted-line shows $x_1/\delta_Z = (Pe_{min})_L$ in Figs. 2-10.

Fig. 3: Variation of $\left[\overline{\rho(\omega_i - \widetilde{\omega}_i)^2}/\bar{\rho}\right]^{1/2} \times \delta_Z/S_L$ (——), $\left[\overline{\rho(\omega_1 - \widetilde{\omega}_1)^2}/\bar{\rho}\right]^{1/2} \times \delta_Z/S_L$ (——), $\left[\overline{\rho(\omega_2 - \widetilde{\omega}_2)^2}/\bar{\rho}\right]^{1/2} \times \delta_Z/S_L$ (——) and $\left[\overline{\rho(\omega_3 - \widetilde{\omega}_3)^2}/\bar{\rho}\right]^{1/2} \times \delta_Z/S_L$(——) with x_1/δ_Z (log scale) for cases A, C and E (1st -3rd column) at $t = 2\,\delta_z/S_L$, $6\,\delta_z/S_L$ and $10\,\delta_z/S_L$ (1st -3rd row).

Fig. 4: Variations of $\overline{(t_{1t}t_{1t})^{1/2}} \times \delta_Z^2/S_L^2$ (——), $\overline{(t_{21t}t_{21t})^{1/2}} \times \delta_Z^2/S_L^2$ (——), $\overline{(t_{22t}t_{22t})^{1/2}} \times \delta_Z^2/S_L^2$(– – –), $\overline{(t_{3t}t_{3t})^{1/2}} \times \delta_Z^2/S_L^2$ (——) and $\overline{(t_{4t}t_{4t})^{1/2}} \times \delta_Z^2/S_L^2$ (——) (log scale) with x_1/δ_Z (log scale) for cases A, C and E (1st -3rd column) at $t = 2\,\delta_z/S_L$, $6\,\delta_z/S_L$ and $10\,\delta_z/S_L$ (1st -3rd row).

Fig. 5: Variations of $\overline{(t_{1n}t_{1n})^{1/2}} \times \delta_Z^2/S_L^2$ (——), $\overline{(t_{21n}t_{21n})^{1/2}} \times \delta_Z^2/S_L^2$ (——), $\overline{(t_{22n}t_{22n})^{1/2}} \times \delta_Z^2/S_L^2$ (– – –), $\overline{(t_{3n}t_{3n})^{1/2}} \times \delta_Z^2/S_L^2$ (——) and $\overline{(t_{4n}t_{4n})^{1/2}} \times \delta_Z^2/S_L^2$ (——) (log scale) with x_1/δ_Z (log scale) for cases A, C and E (1st-3rd column) at $t = 2\,\delta_z/S_L$, $6\,\delta_z/S_L$ and $10\,\delta_z/S_L$ (1st -3rd row).

Fig. 6: Variations of $T_I \times \delta_Z^3/S_L^3$ (——), $T_{II} \times \delta_Z^3/S_L^3$ (——), $T_{III} \times \delta_Z^3/S_L^3$ (– – –), $T_{IV} \times \delta_Z^3/S_L^3$ (——), $T_V \times \delta_Z^3/S_L^3$ (——), $T_{VI} \times \delta_Z^3/S_L^3$ (– – –) and $\bar{D}\,\bar{\Omega}/\bar{D}t \times \delta_Z^3/S_L^3$ (– – –) with x_1/δ_Z (log scale) for case A (1st -2nd column) at $t = 2\,\delta_z/S_L$, $6\,\delta_z/S_L$ and $10\,\delta_z/S_L$ (1st -3rd row).

Fig. 7: Variations of $T_I \times \delta_Z^3/S_L^3$ (——), $T_{II} \times \delta_Z^3/S_L^3$ (——), $T_{III} \times \delta_Z^3/S_L^3$ (– – –), $T_{IV} \times \delta_Z^3/S_L^3$ (——), $T_V \times \delta_Z^3/S_L^3$ (——), $T_{VI} \times \delta_Z^3/S_L^3$ (– – –) and $\bar{D}\,\bar{\Omega}/\bar{D}t \times \delta_Z^3/S_L^3$ (– – –) with x_1/δ_Z (log scale) for case E (1st -2nd column) at $t = 2\,\delta_z/S_L$, $6\,\delta_z/S_L$ and $10\,\delta_z/S_L$ (1st -3rd row).

Fig. 8: Variations of $\overline{\Psi_\alpha} = \overline{|\cos\theta_\alpha|}$ (——), $\overline{\Psi_\beta} = \overline{|\cos\theta_\beta|}$ (——) and $\overline{\Psi_\gamma} = \overline{|\cos\theta_\gamma|}$ (——) with x_1/δ_Z (log scale) for cases A, C and E (1st -3rd column) at $t = 2\,\delta_z/S_L$, $6\,\delta_z/S_L$ and $10\,\delta_z/S_L$ (1st -3rd row).

Fig. 9: Variations of $T_{III} \times \delta_Z^3/S_L^3$ (– – –), $\overline{(\mu/\rho)\nabla^2\Omega} \times \delta_Z^3/S_L^3$ (——), $\overline{(\mu/3\rho)\vec{\omega}\cdot[\nabla\times\nabla(\nabla\cdot\vec{u})]} \times \delta_Z^3/S_L^3$ (——), and $(-D_v) \times \delta_Z^3/S_L^3$ (——) with x_1/δ_Z (log scale) for case A (1st -2nd column) at $t = 2\,\delta_z/S_L$, $6\,\delta_z/S_L$ and $10\,\delta_z/S_L$ (1st -3rd row).

Fig. 10: Variations of $T_{III} \times \delta_Z^3/S_L^3$ (– – –), $\overline{(\mu/\rho)\nabla^2\Omega} \times \delta_Z^3/S_L^3$ (——), $\overline{(\mu/3\rho)\vec{\omega}\cdot[\nabla\times\nabla(\nabla\cdot\vec{u})]} \times \delta_Z^3/S_L^3$ (——), and $(-D_v) \times \delta_Z^3/S_L^3$ (——) with x_1/δ_Z (log scale) for case E (1st -2nd column) at $t = 2\,\delta_z/S_L$, $6\,\delta_z/S_L$ and $10\,\delta_z/S_L$ (1st -3rd row).

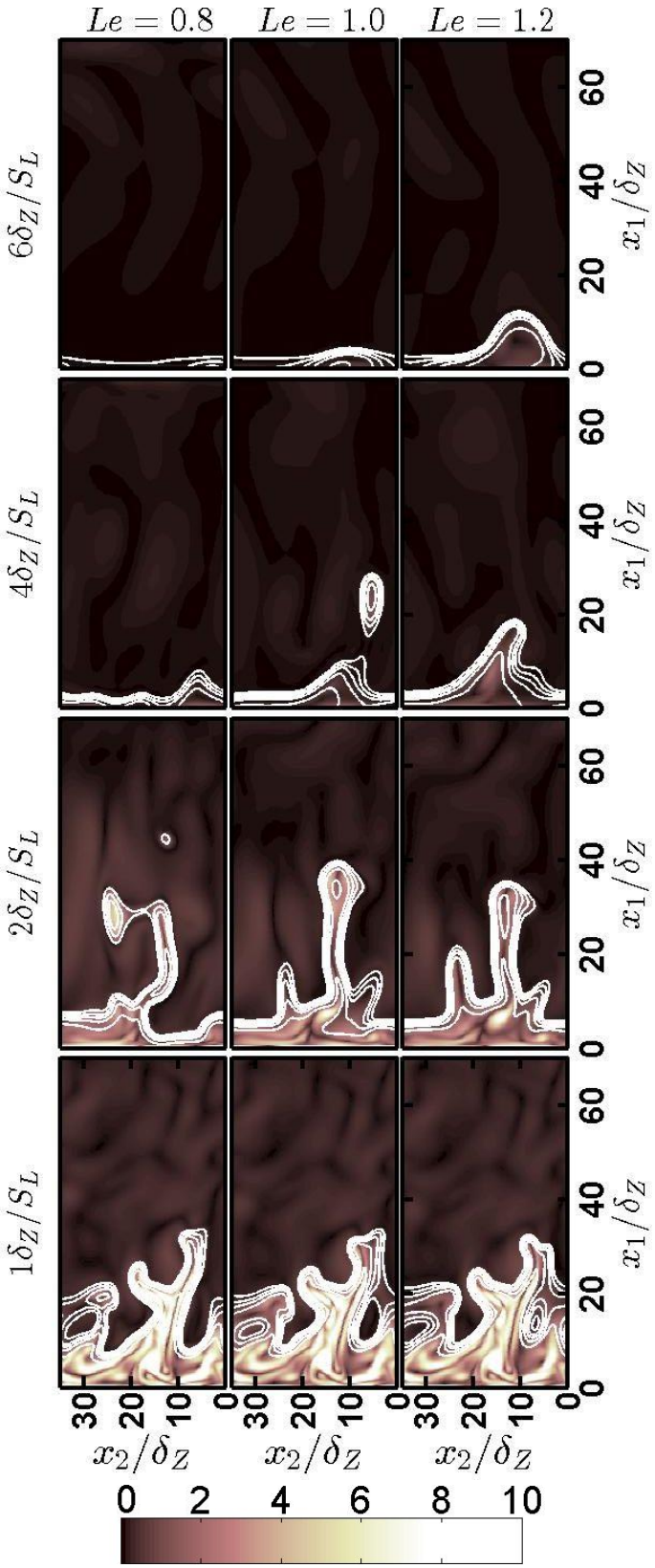

Fig. 1: Distribution of $(\omega_i\omega_i)^{1/2} \times \delta_Z/S_L$ and c (white line from 0.1 to 0.9 with step of 0.2 from bottom to top) fields on $x_1 - x_2$ mid plane for turbulent case E with $Le = 0.8$, 1.0 and 1.2 at t = 1, 2 and $4\delta_Z/S_L$.

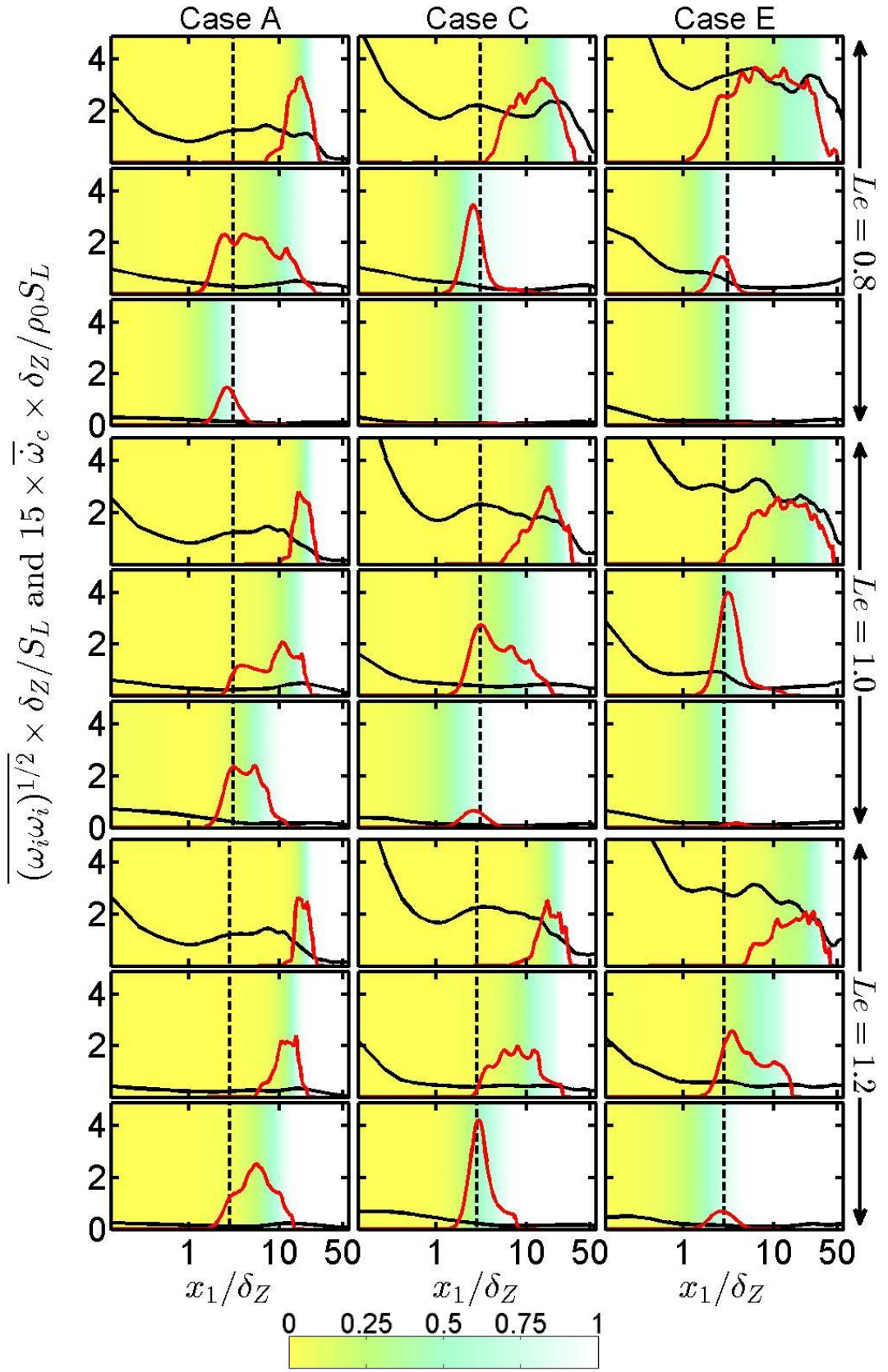

Fig. 2: Variation of $\overline{(\omega_\iota\omega_\iota)^{1/2}} \times \delta_Z/S_L$ (——), $15 \times \bar{\dot{\omega}}_c \times \delta_Z/\rho_0 S_L$ (——) and $\tilde{c}$ with x_1/δ_Z for cases A, C and E at $t = 2\,\delta_z/S_L, 6\,\delta_z/S_L$ and $10\,\delta_z/S_L$ (1st -3rd row). For illustration purpose $\tilde{c}$ is indicated by background colour and the vertical dotted-line shows $x_1/\delta_Z = (Pe_{min})_L$ in Figs. 2-10.

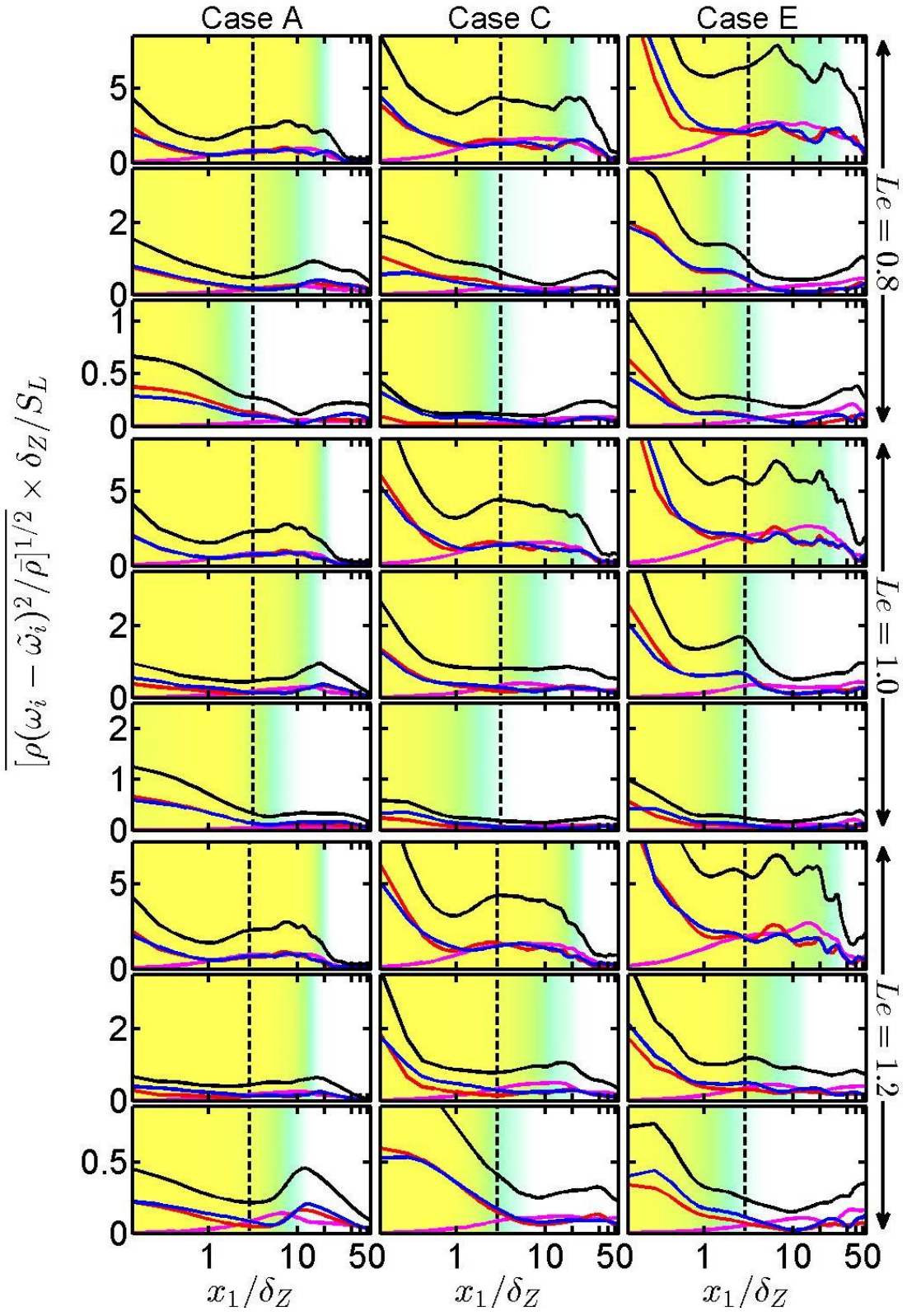

Fig. 3: Variation of $\left[\overline{\rho(\omega_\iota - \widetilde{\omega}_\iota)^2}/\overline{\rho}\right]^{1/2} \times \delta_Z/S_L$ (——), $\left[\overline{\rho(\omega_1 - \widetilde{\omega}_1)^2}/\overline{\rho}\right]^{1/2} \times \delta_Z/S_L$ (——), $\left[\overline{\rho(\omega_2 - \widetilde{\omega}_2)^2}/\overline{\rho}\right]^{1/2} \times \delta_Z/S_L$ (——) and $\left[\overline{\rho(\omega_3 - \widetilde{\omega}_3)^2}/\overline{\rho}\right]^{1/2} \times \delta_Z/S_L$ (——) with x_1/δ_Z (log scale) for cases A, C and E (1st -3rd column) at $t = 2\,\delta_z/S_L$, $6\,\delta_z/S_L$ and $10\,\delta_z/S_L$ (1st -3rd row).

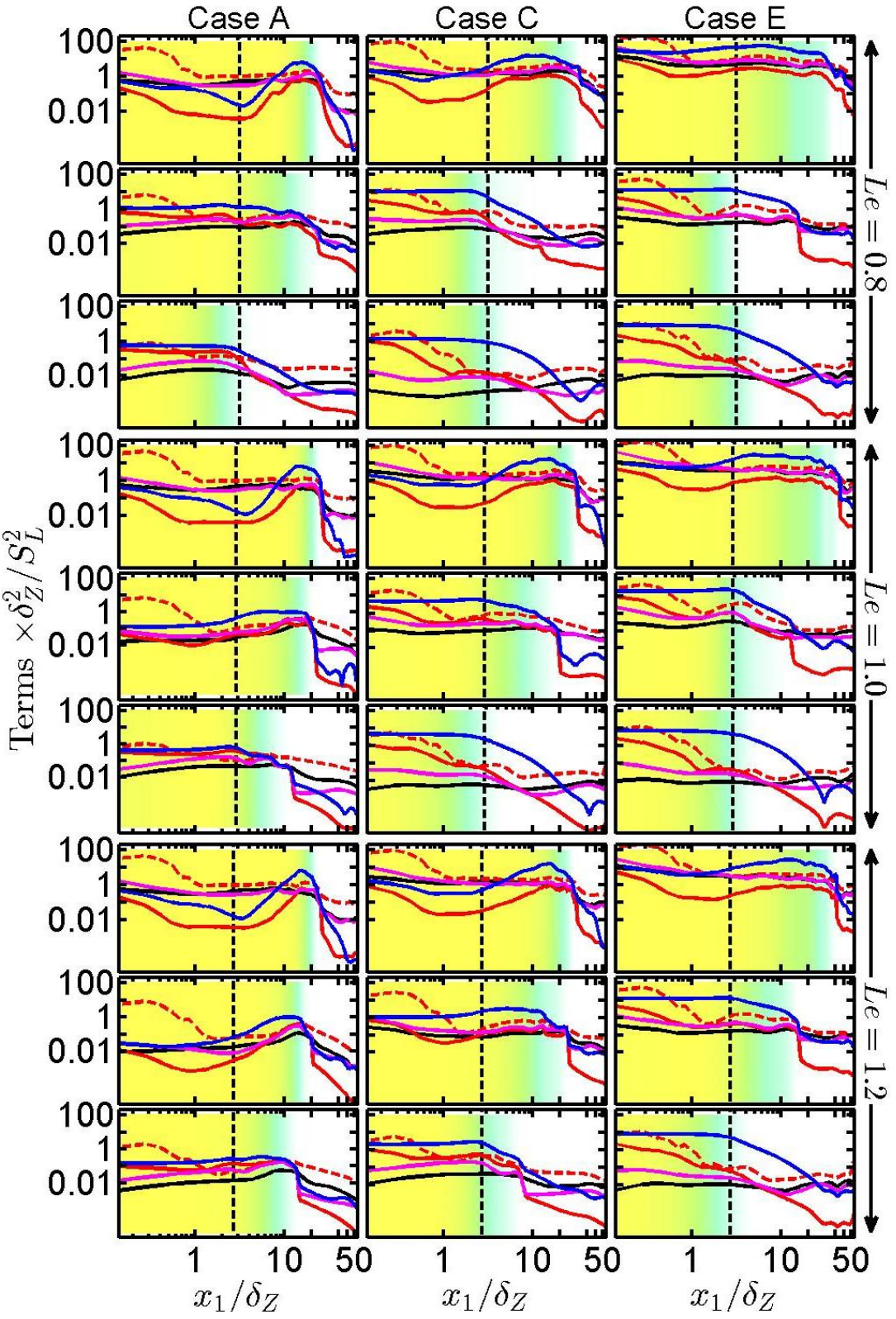

Fig. 4: Variations of $\overline{(t_{1t}t_{1t})^{1/2}} \times \delta_Z^2/S_L^2$ (——), $\overline{(t_{21t}t_{21t})^{1/2}} \times \delta_Z^2/S_L^2$ (——), $\overline{(t_{22t}t_{22t})^{1/2}} \times \delta_Z^2/S_L^2$ (– – –), $\overline{(t_{3t}t_{3t})^{1/2}} \times \delta_Z^2/S_L^2$ (——) and $\overline{(t_{4t}t_{4t})^{1/2}} \times \delta_Z^2/S_L^2$ (——) (log scale) with x_1/δ_Z (log scale) for cases A, C and E (1st -3rd column) at $t = 2\,\delta_z/S_L$, $6\,\delta_z/S_L$ and $10\,\delta_z/S_L$ (1st -3rd row).

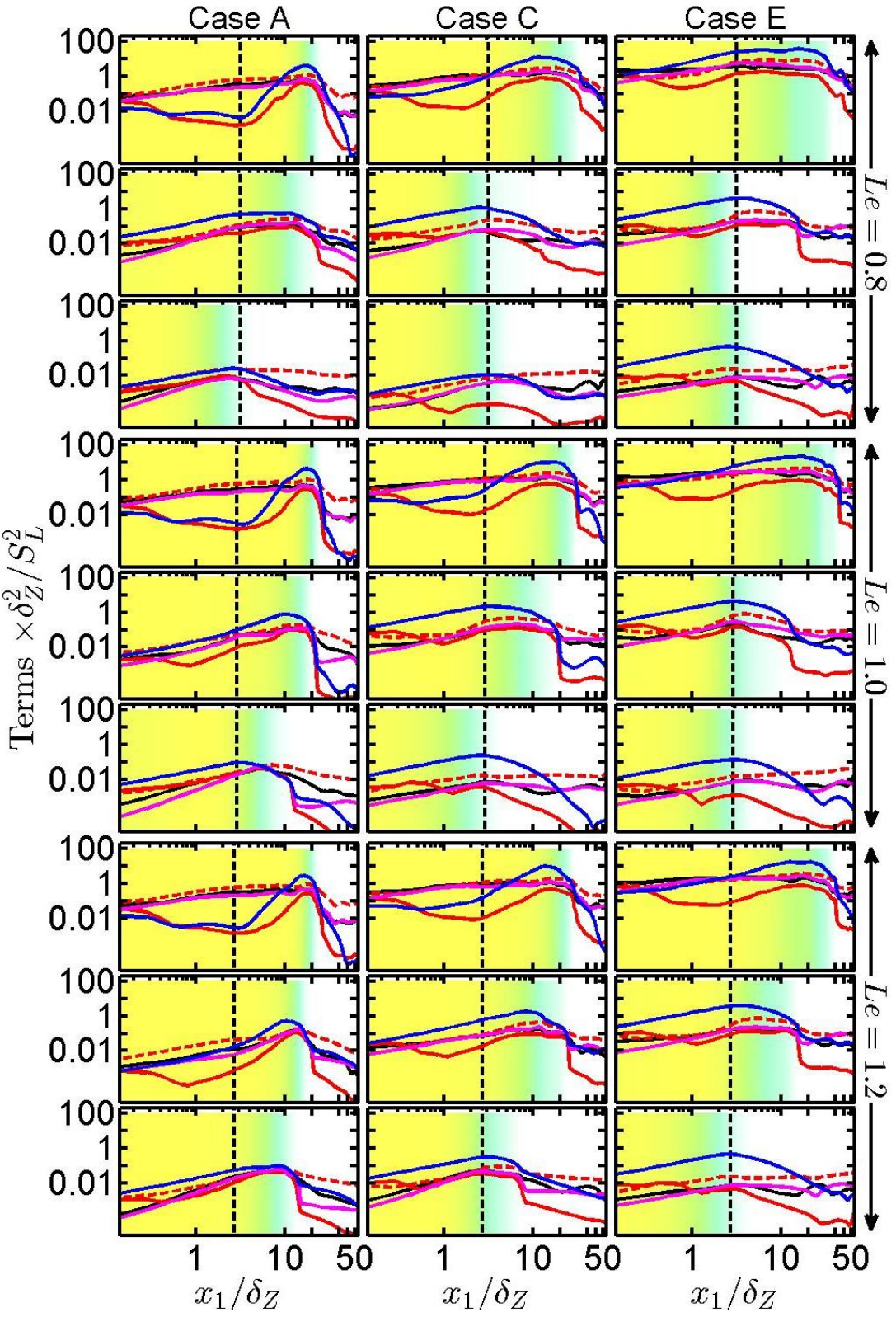

Fig. 5: Variations of $\overline{(t_{1n}t_{1n})^{1/2}} \times \delta_Z^2/S_L^2$ (——) , $\overline{(t_{21n}t_{21n})^{1/2}} \times \delta_Z^2/S_L^2$ (——), $\overline{(t_{22n}t_{22n})^{1/2}} \times \delta_Z^2/S_L^2$ (– – –), $\overline{(t_{3n}t_{3n})^{1/2}} \times \delta_Z^2/S_L^2$ (——) and $\overline{(t_{4n}t_{4n})^{1/2}} \times \delta_Z^2/S_L^2$ (——) (log scale) with x_1/δ_Z (log scale) for cases A, C and E (1st-3rd column) at $t = 2\,\delta_z/S_L$, $6\,\delta_z/S_L$ and $10\,\delta_z/S_L$ (1st -3rd row).

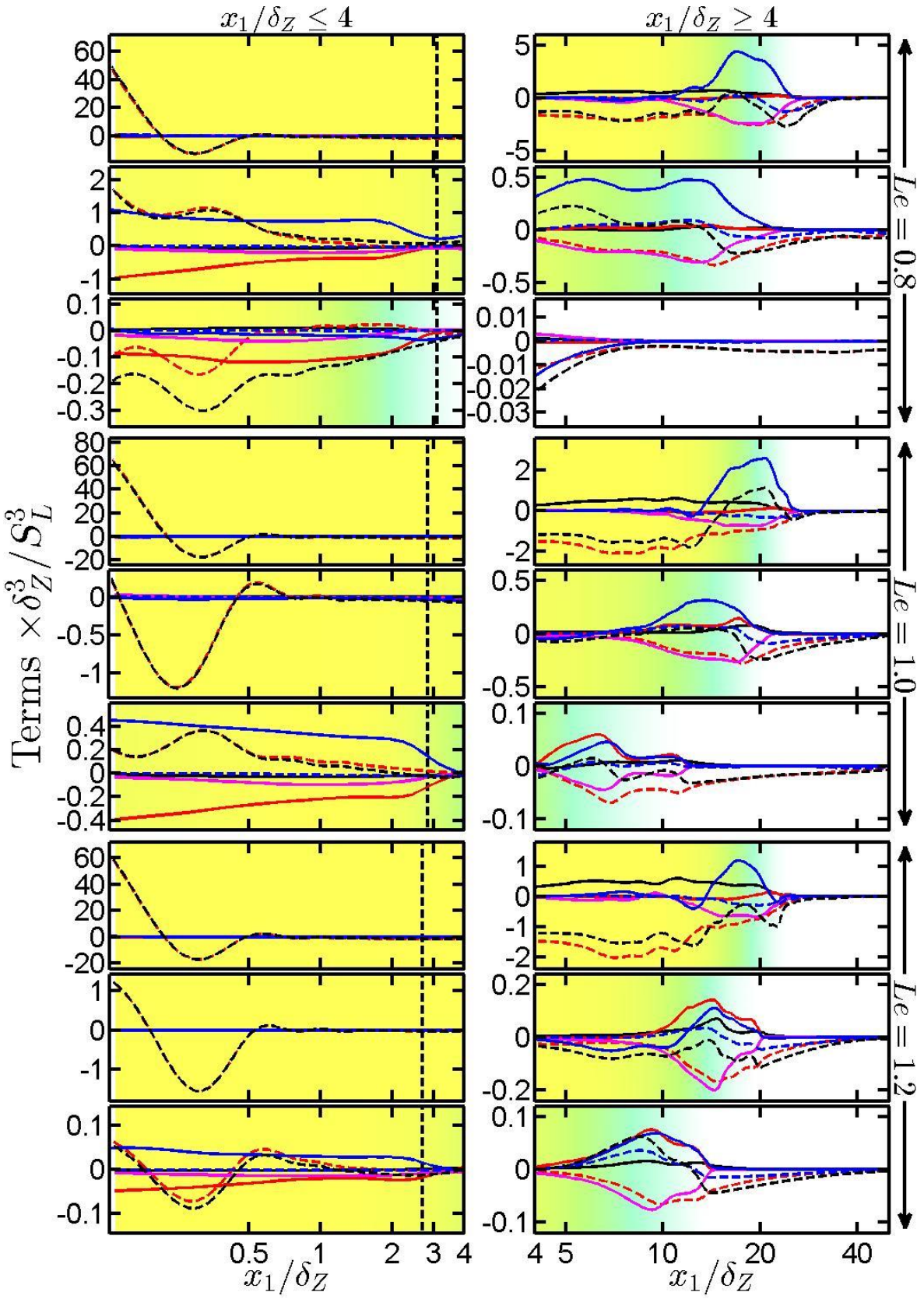

Fig. 6: Variations of $T_I \times \delta_Z^3/S_L^3$ (——), $T_{II} \times \delta_Z^3/S_L^3$ (——), $T_{III} \times \delta_Z^3/S_L^3$ (– – –), $T_{IV} \times \delta_Z^3/S_L^3$ (——), $T_V \times \delta_Z^3/S_L^3$ (——), $T_{VI} \times \delta_Z^3/S_L^3$ (– – –) and $\bar{D}\,\bar{\Omega}/\bar{D}t \times \delta_Z^3/S_L^3$ (– – –) with x_1/δ_Z (log scale) for case A at $t = 2\,\delta_z/S_L$, $6\,\delta_z/S_L$ and $10\,\delta_z/S_L$ (1st -3rd row).

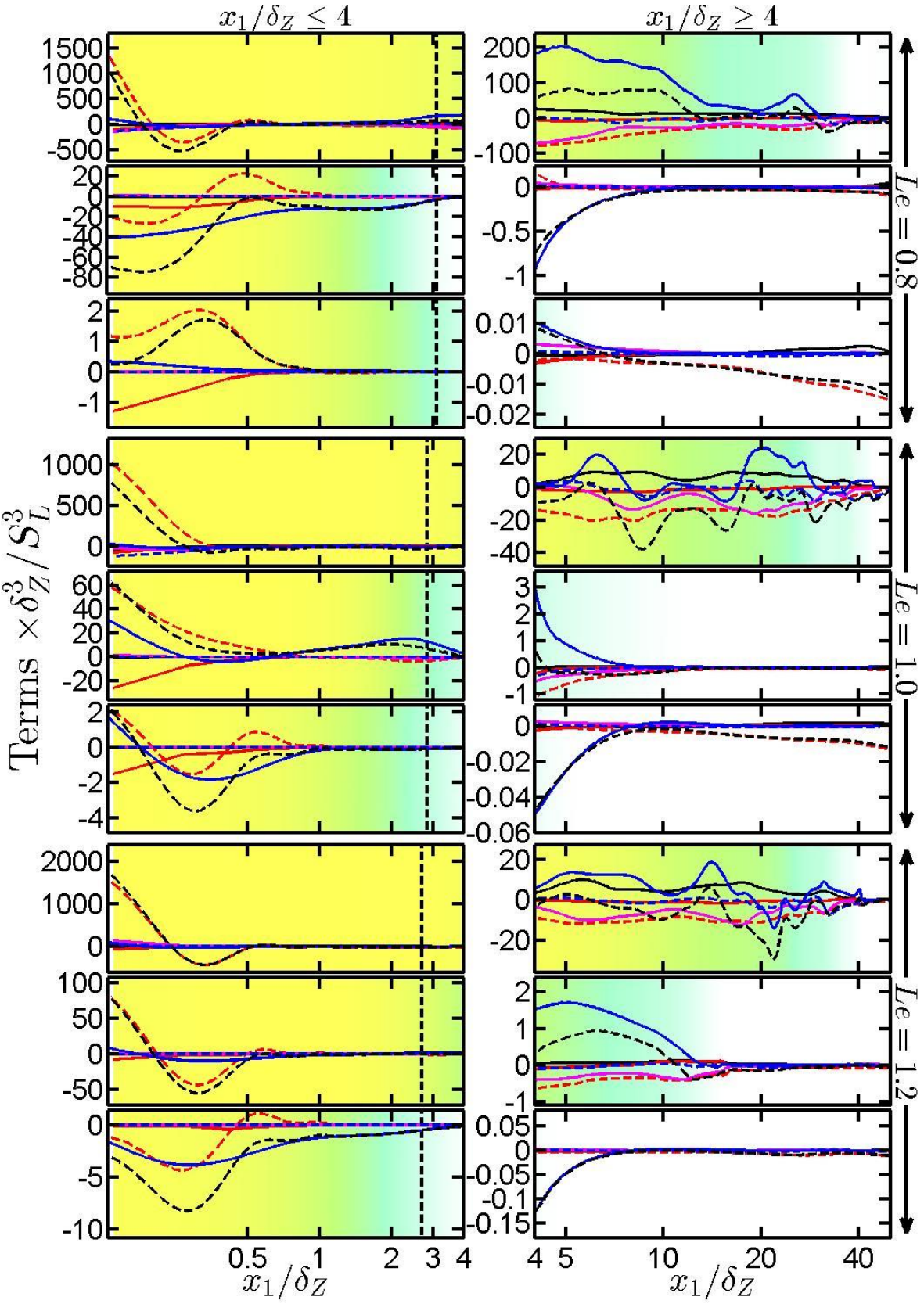

Fig. 7: Variations of $T_I \times \delta_Z^3/S_L^3$ (——), $T_{II} \times \delta_Z^3/S_L^3$ (——), $T_{III} \times \delta_Z^3/S_L^3$ (– – –), $T_{IV} \times \delta_Z^3/S_L^3$ (——), $T_V \times \delta_Z^3/S_L^3$ (——), $T_{VI} \times \delta_Z^3/S_L^3$ (– – –) and $\bar{D}\,\bar{\Omega}/\bar{D}t \times \delta_Z^3/S_L^3$ (— —) with x_1/δ_Z (log scale) for case E at $t = 2\,\delta_z/S_L$, $6\,\delta_z/S_L$ and $10\,\delta_z/S_L$ (1st -3rd row).

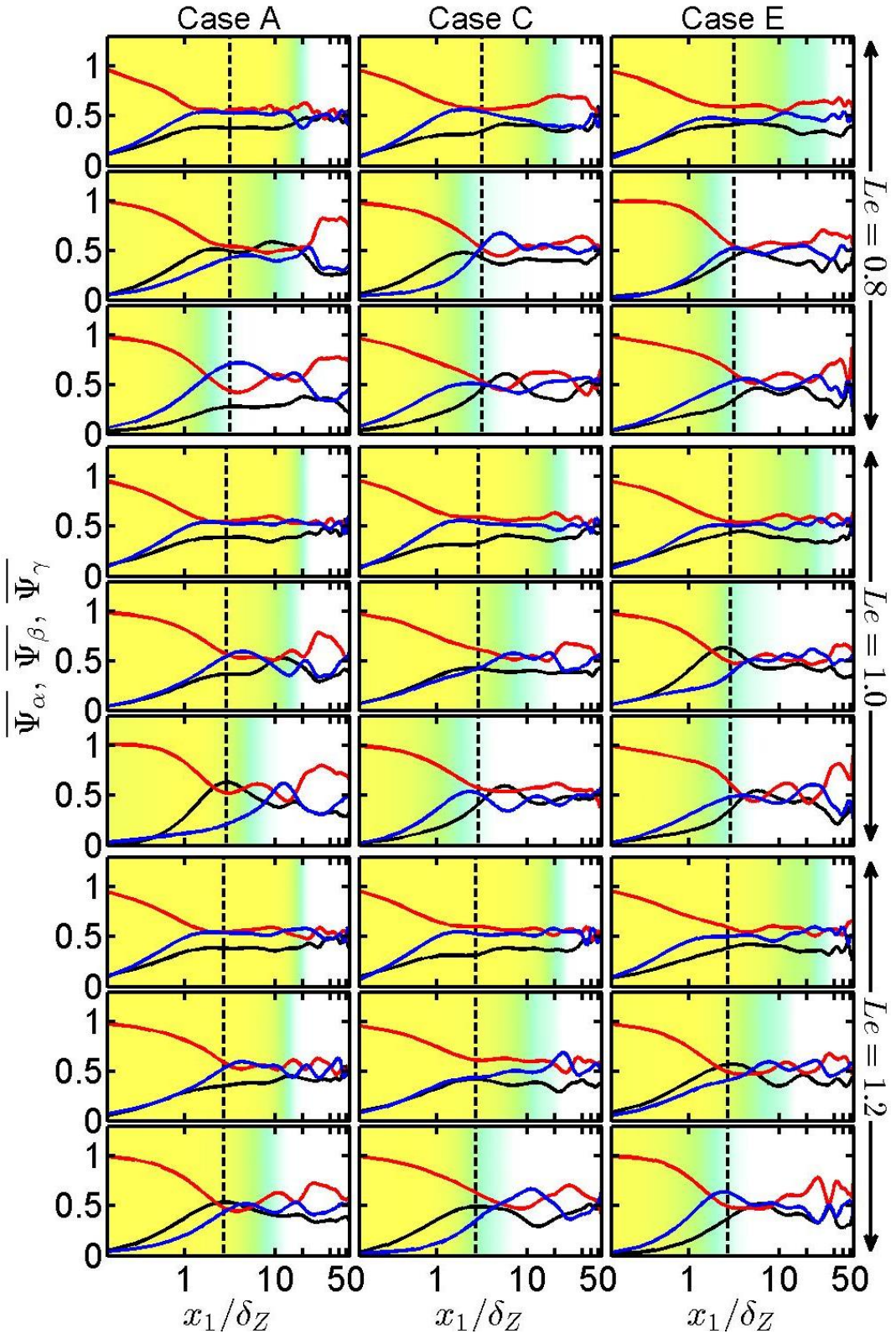

Fig. 8: Variations of $\overline{\Psi_\alpha} = \overline{|\cos\theta_\alpha|}$ (——), $\overline{\Psi_\beta} = \overline{|\cos\theta_\beta|}$(——) and $\overline{\Psi_\gamma} = \overline{|\cos\theta_\gamma|}$ (——) with x_1/δ_Z (log scale) for cases A, C and E (1st -3rd column) at $t = 2\,\delta_z/S_L$, $6\,\delta_z/S_L$ and $10\,\delta_z/S_L$ (1st -3rd row).

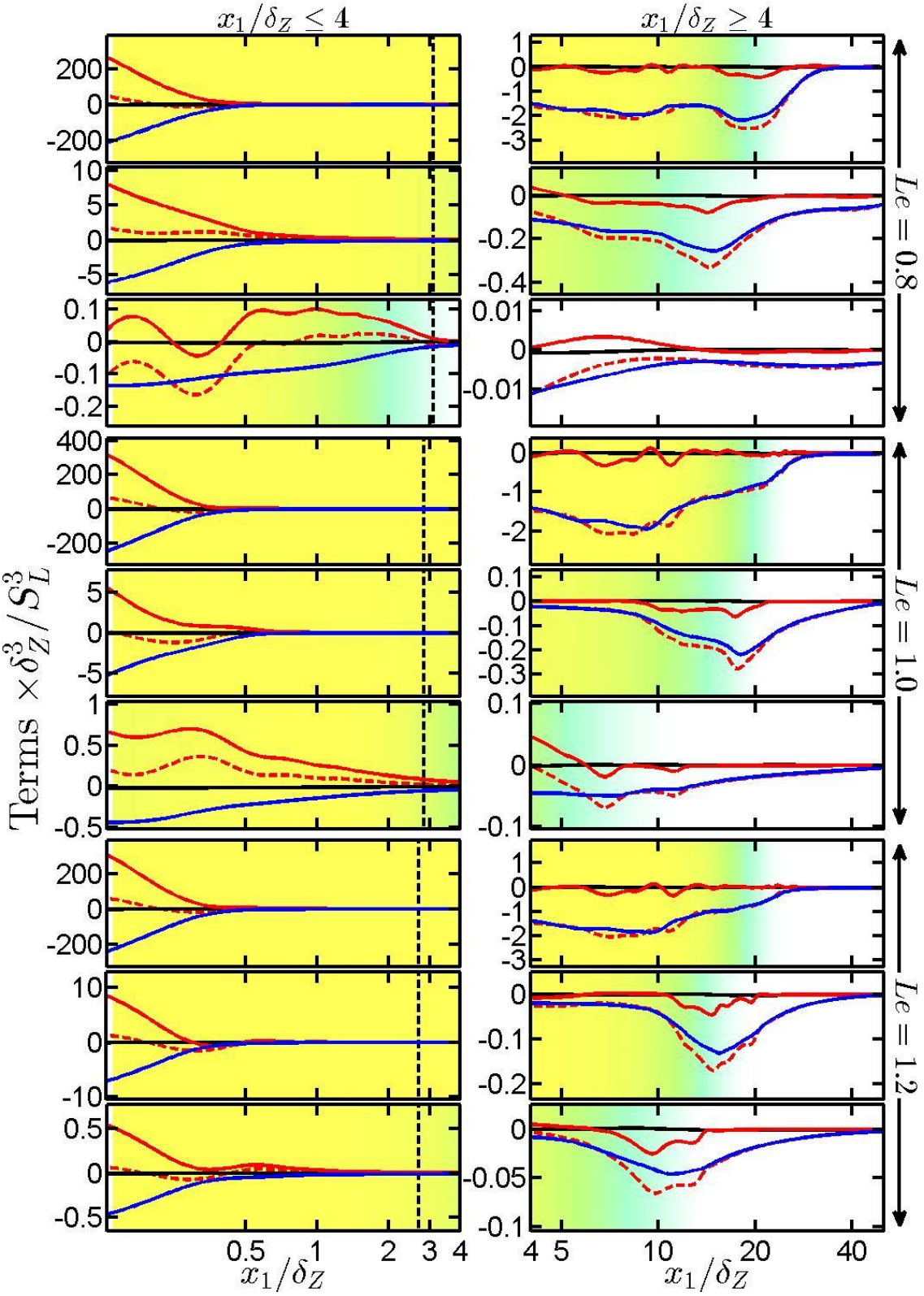

Fig. 9: Variations of $T_{III} \times \delta_Z^3/S_L^3$ (– – –), $\overline{(\mu/\rho)\nabla^2\Omega} \times \delta_Z^3/S_L^3$ (——), $\overline{(\mu/3\rho)\vec{\omega} \cdot [\nabla \times \nabla(\nabla \cdot \vec{u})]} \times \delta_Z^3/S_L^3$ (——), and $(-D_v) \times \delta_Z^3/S_L^3$ (——) with x_1/δ_Z (log scale) for case A at $t = 2\,\delta_z/S_L$, $6\,\delta_z/S_L$ and $10\,\delta_z/S_L$ (1st -3rd row).

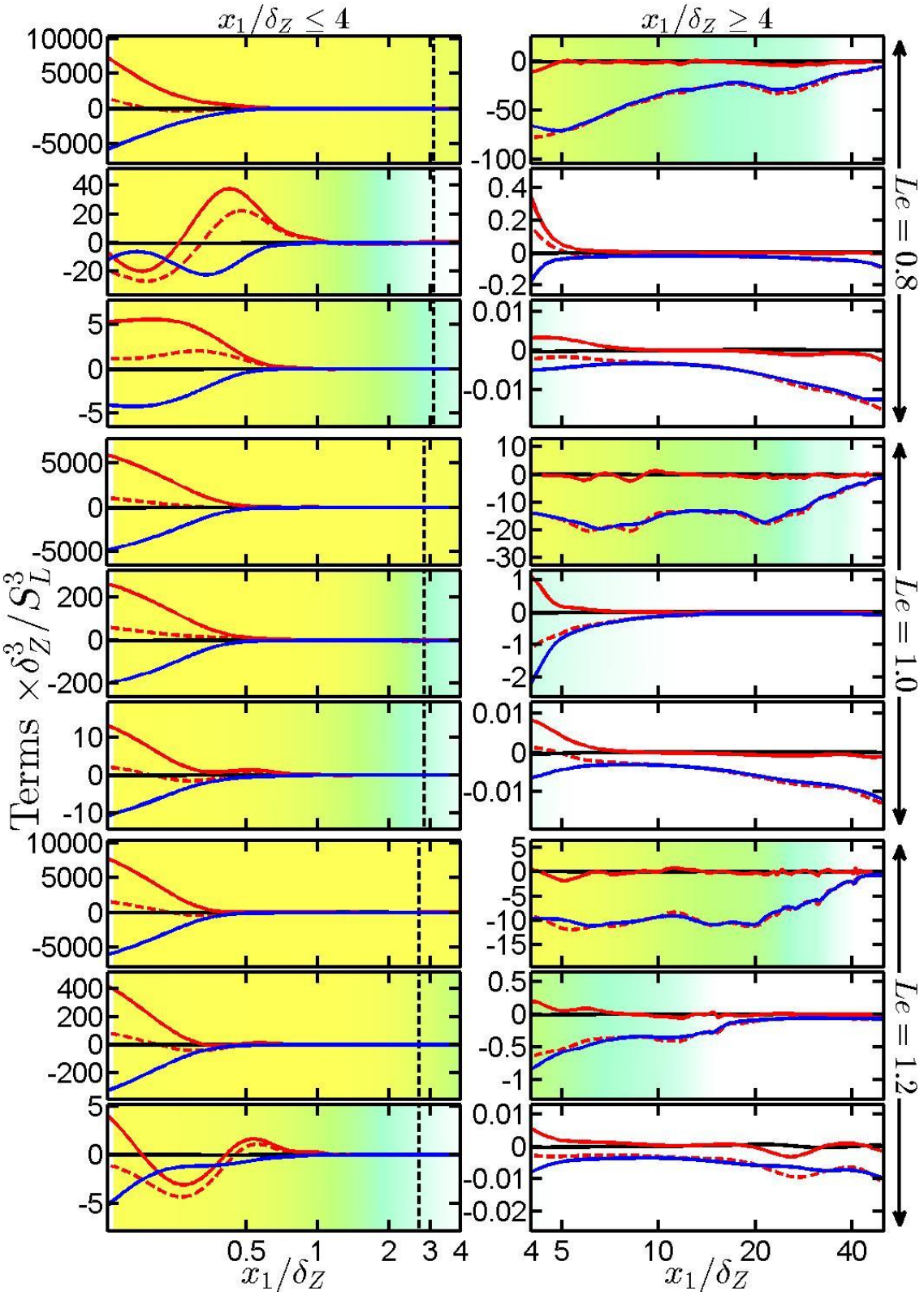

Fig. 10: Variations of $T_{III} \times \delta_Z^3/S_L^3$ (– – –), $\overline{(\mu/\rho)\nabla^2\Omega} \times \delta_Z^3/S_L^3$ (——), $\overline{(\mu/3\rho)\vec{\omega}\cdot[\nabla\times\nabla(\nabla\cdot\vec{u})]} \times \delta_Z^3/S_L^3$ (——), and $(-D_v) \times \delta_Z^3/S_L^3$ (——) with x_1/δ_Z (log scale) for case E at $t = 2\,\delta_z/S_L$, $6\,\delta_z/S_L$ and $10\,\delta_z/S_L$ (1st -3rd row).